Journal of Geophysical Research: Atmospheres

RESEARCH ARTICLE
10.1029/2018JD029474

Contemporary GCM Fidelity in Representing the Diurnal Cycle of Precipitation Over the Maritime Continent

Dariusz B. Baranowski[1,2,3], Duane E. Waliser[1,2], Xianan Jiang[1,2], James A. Ridout[4], and Maria K. Flatau[4]

[1]Joint Institute for Regional Earth System Science and Engineering, University of California, Los Angeles, CA, USA, [2]Jet Propulsion Laboratory, California Institute of Technology, Pasadena, CA, USA, [3]Institute of Geophysics, Polish Academy of Sciences, Warsaw, Poland, [4]Naval Research Laboratory, Monterey, CA, USA

Key Points:
- GCMs are sensitive to the existence of the Maritime Continent in the Indo-Pacific warm pool
- Most models underestimate daily mean precipitation and amplitude of the diurnal cycle, especially over land
- Most GCMs underestimate land-sea contrast in precipitation characteristics

Correspondence to:
D. B. Baranowski,
dbarnaowski@igf.edu.pl

Citation:
Baranowski, D. B., Waliser, D. E., Jiang, X., Ridout, J. A., & Flatau, M. K. (2019). Contemporary GCM fidelity in representing the diurnal cycle of precipitation over the Maritime Continent. *Journal of Geophysical Research: Atmospheres*, *124*, 747–769. https://doi.org/10.1029/2018JD029474

Received 14 AUG 2018
Accepted 1 DEC 2018
Accepted article online 9 DEC 2018
Published online 28 JAN 2019

Abstract This paper presents a multimodel assessment of fidelity in representation of the diurnal cycle of precipitation over the Maritime Continent (MC). Daily mean precipitation rate and amplitude and phase of the diurnal cycle are utilized to validate General Circulation Model (GCM) performance with respect to multiyear annual mean and seasonal cycle. The analysis shows that models' 6-hourly temporal resolution and 2.5° spatial resolution is sufficient to depict key characteristic of diurnal precipitation. Results show that most models are sensitive to the existence of the MC and show different characteristics of subdaily precipitation. However, 19 out of 20 models underestimate the daily mean precipitation over the eastern Indian Ocean and most of them underestimate both daily mean precipitation and amplitude of the diurnal cycle, especially over islands within the region. Observations show that within the MC the diurnal cycle is higher over land than over ocean. Many models decrease this land-sea contrast. Most models recognize difference in phase of the diurnal cycle between MC islands and surrounding ocean, but some of them show opposite phasing of the diurnal cycle. Results show that modern models perform better than past generation, sometimes comparably to regional models' run in much higher resolution. Although models perform well with respect to the seasonal cycle of the daily mean precipitation, they fail to realistically represent the seasonal evolution of the diurnal cycle amplitude. Additionally, models show no coherence in land-ocean contrast derived from a multiyear average of daily mean precipitation and amplitude of the diurnal cycle.

1. Introduction

The Maritime Continent (MC) is a unique region in the Earth. It is an archipelago between the Indian and Pacific Oceans composed of a mixture of many small and large islands with large topographic features and shallow and deep seas. It is a part of the Indo-Pacific warm pool, a large area with very high sea surface temperature (SST). The importance of the MC region for global weather and climate has long been recognized (Ramage, 1968).

The intraseasonal variability of the tropical circulation is dominated by planetary-scale eastward propagating events known as Madden-Julian Oscillations (MJOs; Madden & Julian, 1972; Zhang, 2005). The MJO exerts significant impacts on global weather and climate (Lau & Waliser, 2011) and represents a dominant source of predictability for the global atmospheric circulation on subseasonal time scales (i.e., Neena et al., 2014; Reichler & Roads, 2005; Waliser et al., 2003).

The MC region creates a natural barrier to the eastward propagation of the MJO (Rui & Wang, 1990; Salby & Hendon, 1994). Although many MJO events weaken, stall, or terminate within the MC region (Rui & Wang, 1990), many general circulation models (GCMs) overestimate this behavior (Jiang et al., 2015; Kim et al., 2009). This bias limits the forecast skill of GCMs and is often referred to as the "predictability barrier" of the MJO by the MC (Seo et al., 2009). However, recently, it was shown that the MJO predictability over the MC is similar to Indian and Pacific Oceans (Neena et al., 2014), which means that prediction skill can be better if models are improved.

The MC is characterized by a vigorous diurnal cycle of convection driven by the difference in heat capacity between ocean and land surfaces and the resulting contrast in surface temperature between islands and surrounding seas (Qian, 2008). The diurnal cycle of convection is the source of fresh water to the MC region and is critically linked with local conditions (e.g., orography) as well as large-scale circulation (Wang & Sobel, 2017). The

diurnal cycle of convection is strongly affected by eastward propagating convection, including that associated with the MJO (Birch et al., 2016; Peatman et al., 2014) and convectively coupled Kelvin waves (Baranowski et al., 2016). These impacts have been shown to be part of multiscale interactions in which the propagation properties of organized atmospheric convection are also impacted (Baranowski et al., 2016; Hagos et al., 2016).

In the modeling context, proper representation of the diurnal cycle of convection over the MC has long been recognized as a challenging task (Ackerley et al., 2014; Neale & Slingo, 2003; Ruppert & Hohenegger, 2018). Although a robust examination of modern GCM performance with respect to the diurnal cycle of convection over the MC region has not been performed, it has been noted that many models struggle with accurate simulations of the amplitude and phase of the diurnal cycle of precipitation, which results in a dry bias over the MC region (Neale & Slingo, 2003). Additionally, it has been suggested that improvements to model representations of the precipitation distribution over the MC require spatial resolutions on the order of 10 km, which is much higher than that in most modern GCMs (Love et al., 2011). Recently, advances in regional MC environment and its variability have been achieved (Hassim et al., 2016; Thompson et al., 2018). High spatial resolution (~5–10 km) mesoscale models are able to resolve differences in diurnal evolution of convection over land and ocean. However, even those simulations suffer from underestimation of the mean diurnal cycle amplitude and some bias in the phase of the diurnal cycle (Hassim et al., 2016).

Recognizing the importance of the multiscale interactions between propagating convection and the local diurnal cycle of precipitation over the MC and opportunity arising from extended range weather predictions, this study focuses on the mean diurnal cycle of convection, a dominant mode in the MC weather because it is critically linked with longer, subseasonal-to-seasonal, time scales. The study presents an assessment of performance of state-of-the-art GCMs with respect to the diurnal cycle and its seasonal variability. The structure of the paper is the following: Section 2 presents data and methodology used in this study, including key metrics, which will be utilized to assess models' performance; section 3 provides an assessment of models' fidelity with respect to the mean diurnal cycle of convection; section 4 analyzes the seasonal cycle of the diurnal cycle of convection and precipitation over the MC region; and section 5 provides a summary and discussion of our results.

2. Data and Methodology

In this paper, we evaluate climate simulations from multiple GCMs. Data from the Tropical Rainfall Measurement Mission (TRMM) 3B42 v7 data set (Huffman et al., 2007) are used as the observational reference. In order to quantify models' performance, we have derived metrics, which correspond well with the key characteristics of the diurnal cycle of precipitation over the MC region. Below we describe the data and methods used in this study.

2.1. GCM Model Data

Recently, the MJO Task Force (MJOTF) and the Global Energy and Water Exchanges (GEWEX) Atmospheric System Study (GASS) developed a modeling experiment to help address issues related to the vertical structure of diabatic processes associated with the MJO and to explore how their structures and fidelity relate to models' MJO representation and forecast skill (Klingaman, Jiang, et al., 2015; Petch et al., 2011). Results from three experimental components of the MJOTF/GASS global model intercomparison have already been published, including (a) a 20-year climate simulation (Jiang et al., 2015), (b) a 2-day hindcast (Xavier et al., 2015), and (c) a 20-day hindcast component (Klingaman, Woolnough, et al., 2015).

This study utilizes surface precipitation rate data from the climate simulation component of the MJOTF/GASS model intercomparison project. In this component, participating models were integrated for 20 years. For atmosphere-only runs, weekly SST and sea ice concentrations based on the National Oceanic and Atmospheric Administration Optimum Interpolation V2 product (Reynolds et al., 2002) for the 20 year period of 1991–2010 were specified as the model lower boundary conditions. Although output from all participating GCMs was supposed to be archived at every 6 hr on standard horizontal (2.5° by 2.5°) grids and 22 vertical pressure levels, subdaily outputs from some models were not provided. Because this study aims at benchmark assessment of diurnal cycle over the MC region, such models were excluded from analysis. For example, the superparameterized version of CAM model (SPCAM), which has been shown to produce realistic diurnal

Table 1
Participating Models With Horizontal/Vertical Resolutions

Model name	Institution	Resolution	Air-sea coupling
ACCESS	Centre for Australian Weather and Climate Research	1.875° × 1.25°, L85	✖
BCCAGCM2.1	Beijing Climate Center, China Meteorological Administration	T42 (2.8°), L26	✖
CAM5ZMMicroCAPT	Lawrence Livermore National Laboratory	1.25° × 0.9°, L30	✖
CanCM4	Canadian Centre for Climate Modeling and Analysis	2.8°, L35	✓
CNRMa	Centre National de la Recherche Scientifique/Météo-France	T127 (1.4°), L31	✖
CNRMb			✓
CNRMc			✖/✓
CWBGFS	Central Weather Bureau, Taiwan	T119 (1°), L40	✖
ECEarth3	Rossby Centre, Swedish Meteorological and Hydrological Institute	T255 (80 km), L91	✖
ECGEM	Environment Canada	1.4°, L64	✖
FGOALSs	Institute of Atmospheric Physics, Chinese Academy of Sciences	T42 (2.8°), L26	✖
GEOS5_AGCM	Global Modeling and Assimilation Office, NASA	0.625° × 0.5°, L72	✖
ISUGCM	Iowa State University	T42 (2.8°), L26	✖
MIROC5	AORI/NIES/JAMSTEC, Japan	T85 (1.5°), L40	✖
ModelE	Goddard Institute for Space Studies, NASA	2.5° × 2.0°, L40	✖
MRI-AGCM	Meteorological Research Institute, Japan	1.875° × 1.25°, L85	✖
NCAR-CAM5	National Center for Atmospheric Research	1.25° × 0.9°, L30	✖
NCHU	Academia Sinica, Taiwan	T63 (2°), L31	✓
NGEM01	U.S. Naval Research Laboratory	T359 (37 km), L42	✖
TAMU-CAM4	Texas A&M University	2.5° × 1.9°, L26	✖

cycle (Pritchard & Somerville, 2009), is part of the GASS/YoTC data set, but it did not provide subdaily data and thus is excluded from this study. For more details about the MJOTF/GASS modeling experiment, readers are referred to the project website: http://www.ucar.edu/yotc/mjodiab.html.

The list of models and the variables used in this study, along with the horizontal and vertical resolutions used in each model, are given in Table 1. There are 20 simulations from 18 GCMs. While most of the models analyzed in this study are atmosphere-only models (AGCMs), three of the models were integrated as coupled atmosphere-ocean systems (CGCMs; indicated in rightmost column in Table 1). Also noteworthy is that three simulations were conducted based on the CNRM GCM, including an AGCM integration forced by the observed weekly SST and sea ice (CNRMa), a fully atmosphere-ocean coupled CGCM run (CNRMb), and a third experiment in which the AGCM was forced by the monthly mean SST and sea ice output from the coupled run (CNRMc). Another noteworthy model is the TAMU-CAM4, in which the "observed" latent heating structure for the MJO based on TRMM estimates was used to constrain both the horizontal and vertical distribution of model heating throughout the tropics (Lappen & Schumacher, 2012). It was found that the model MJO is significantly improved over the original CAM after applying this technique (Jiang et al., 2015; Lappen & Schumacher, 2012, 2014).

2.2. TRMM Verification Data Set

The TRMM 3B42 v7 data set provides estimates of surface precipitation rate with relatively high spatial (~ 0.25°) and temporal (3-hourly) resolutions. We use these data from a full 15-year-long period (1998–2013) as the observational reference. Although direct observations (satellite-borne radar) used to generate TRMM 3B42 data are infrequent and heavily rely on passive satellite retrieval methods (merged infrared and microwave data), we use long period and first calculate multiyear averages and their standard deviations. Additionally, we average native TRMM data to reduce its spatial and temporal resolution down to the resolution of the GCMs' output. We will refer to these two data sets as high-resolution (HiRes) and low-resolution (LoRes) TRMM. Hence, HiRes TRMM has 0.25° spatial and 3-hourly temporal resolution, whereas LoRes TRMM

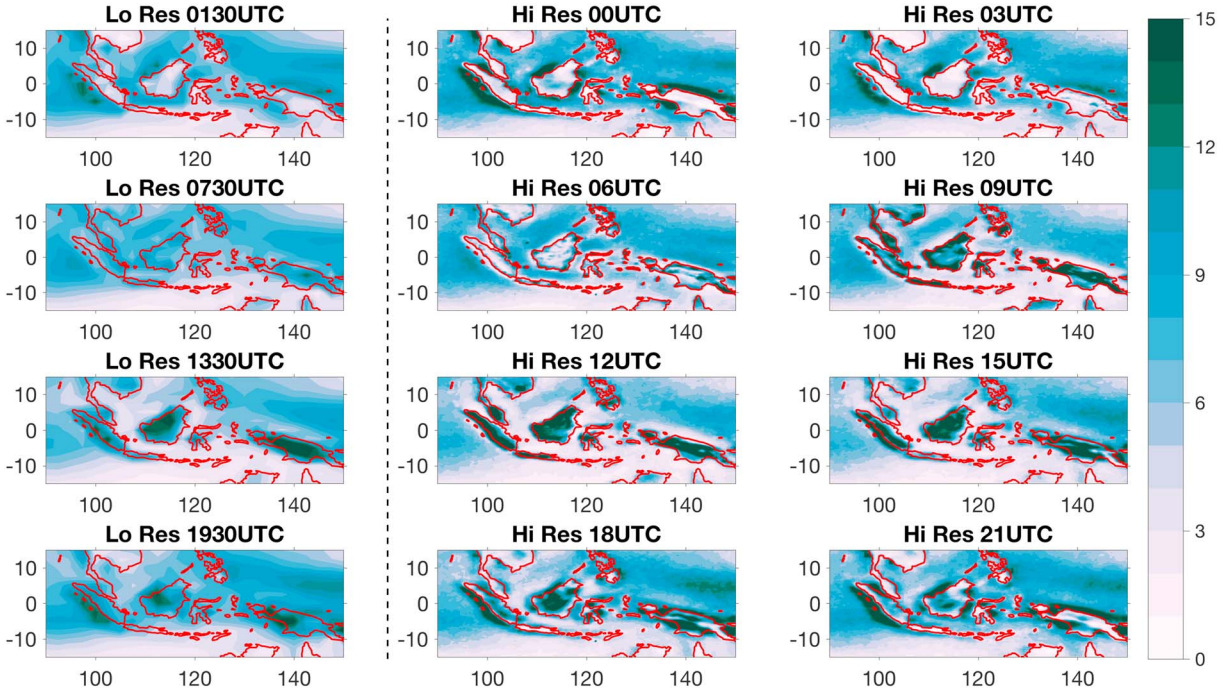

Figure 1. Precipitation rate (mm/day) from TRMM 3B42v7 data at native (high-resolution HiRes; middle and right columns) and models' (low-resolution, LoRes; left column) resolutions. The time marked above each panel is in UTC. To transform it to local solar time, one should add between 6 hr at 90°E and 10 hr at 150°E.

has 2.5° spatial and 6-hourly temporal resolution, with the latter equal to the common resolution of the MJOTF/GASS model outputs.

First, we demonstrate that the LoRes TRMM data exhibit a substantive enough imprint of the diurnal cycle of precipitation that it can be useful for model evaluation. Previous studies have shown that the diurnal cycle of precipitation has distinct characteristics over the MC, recognizable from high spatial resolution HiRes TRMM (Oh et al., 2012; Peatman et al., 2014) and CMORPH data (Qian, 2008). The key feature exhibited in those studies is high spatial and temporal inhomogeneity in the precipitation distribution within the MC region. This feature is observed throughout the year but modulated by seasonal and intraseasonal variability. This spatial-temporal pattern is such that precipitation over land parts of the region (i.e., islands) reaches a maximum in late afternoon/evening (local solar time afternoon—p.m.) and a minimum at night/early morning (local solar time morning—a.m.). In contrast, precipitation over the seas surrounding the islands is peaked at night/early morning and shows a minimum during afternoon/early evening.

Previous analyses (e.g., Peatman et al., 2014) were based on the high-resolution data sets (e.g., temporal resolution 3 hr or better, spatial resolution 50 km or better). The question therefore arises if the degraded resolution data set is able to capture the spatial structure of ocean-land differences in precipitation pattern. To this end we present Figure 1, in which the middle and right columns show multiyear mean precipitation for each available 3-hourly interval (note that time is UTC; to transform it to local solar time add between 6 hr at 90°E to 10 hr at 150°E; this figure is in UTC because data are provided at UTC intervals). The fine structure of the precipitation distribution is exemplified by rapid onset of precipitation over islands close to the coast during local solar time afternoon (09–12 UTC) and its enhancement inland during the following hours (12–15 UTC) and a decay over the evening (18–21 UTC). Local solar time morning (00–03 UTC) is characterized by virtually no precipitation over land. The decaying precipitation over islands coincides with increasing precipitation over adjacent seas. Over ocean, precipitation first occurs near the coast (18–21 UTC), later enhances and propagates offshore (00–03 UTC), and decays around local solar time noon (06 UTC). Such progression is common for land masses of Borneo, New Guinea, Java, and Celebes. For Sumatra the offshore propagation occurs a little sooner. The maximum precipitation propagates westward off the coast of the island around local solar time midnight (18 UTC). At that time near

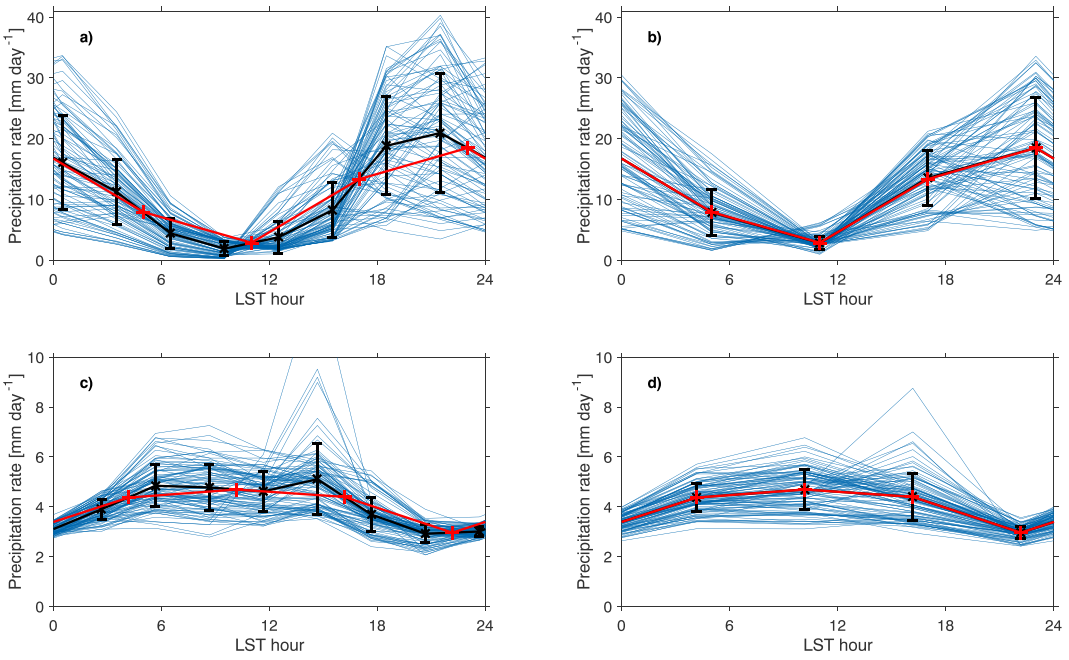

Figure 2. Effects of temporal and spatial averaging between high-resolution (HiRes) and low-resolution (LoRes) TRMM data based on the mean diurnal cycle in New Guinea (142.5°E and 5°S; a and b) and Banda Sea (130°E and 7.5°S; c and d). Each blue line in all panels represents the diurnal evolution at one of 100 grid points used for averaging. Panels (a) and (c) show effects of spatial averaging; blue lines are original 3-hourly data, black line shows mean, and black bars show standard deviation of 3-hourly diurnal cycle at the reference location; red line shows LoRes diurnal cycle at the reference location. Panels (b) and (d) show effects of temporal averaging: Blue lines are 6-hr time-averaged data at high spatial resolution, black line shows mean, and black bars show standard deviation of 6-hourly diurnal cycle over the reference location; red line shows LoRes diurnal cycle over the reference location.

Borneo and New Guinea, precipitation is still clearly over land. The different behavior of Sumatra might be attributed to its topography, mainly coastal mountain range, as well as the stretch of the Nias islands over shallow seas parallel to the coast, which act as the island's westward extension and favor offshore propagation of precipitation (Mori et al., 2004).

Most of the key diurnal features described above are still exhibited in the LoRes TRMM data (Figure 1). Although the details of the precipitation onset over land are diminished, the precipitation clustering over land during local solar time afternoon (12–18 UTC) and its confinement to the adjacent seas during local solar time morning (00 UTC) are still evident. It can be seen that the magnitude of the mean precipitation rate is lower and its distribution smoother in LoRes TRMM data in comparison with the high-resolution data. For example, a double rain band over New Guinea (15 UTC in HiRes TRMM data) appears as one large precipitation maximum evenly distributed over the island (1330 UTC in LoRes TRMM data). This double band is a real feature, which exists due to a mountain range that runs across the island along its longer axis (Hassim et al., 2016). On the other hand, there is an excess of precipitation occurring over the west coast of Sumatra in comparison to the Island's east coast, also due to orographic effects of the near coast mountain range barrier (Mori et al., 2004). This feature is well represented in LoRes TRMM data. On the other hand, the diurnal evolution of precipitation over Java Island is much smaller in LoRes data than that in HiRes data due to the location and size of the island, such that in LoRes data precipitation over land is averaged together with surrounding seas. Therefore, the diurnal characteristics of precipitation over land and ocean are averaged together resulting in diminished diurnal evolution over this land mass.

The apparent biases in the LoRes data set in comparison with the HiRes data set result from spatial and temporal averaging. Throughout this paper, we degrade the resolution by averaging in space and time. Spatial averaging is accomplished by averaging 100 individual HiRes (0.25° resolution) grid point data for each LoRes (2.5° resolution) grid box. Averaging in time is done by calculating averages from pairs of HiRes data (e.g., 0000 UTC and 0300 UTC) to obtain a single LoRes value (e.g., 0130 UTC). As a result a single 6-hourly

(four data points per day) LoRes diurnal evolution is calculated from 96 individual 3-hourly (eight data points per day) diurnal evolutions at HiRes. For illustration, Figure 2 shows an example of this technique over two locations: New Guinea and Banda Sea. It can be seen that in both locations individual HiRes evolutions show a clear diurnal signal with coherent phase. However, the amplitude of the diurnal cycle is much larger over land than over ocean. Over a land location (Figures 2a and 2b) maximum precipitation is observed between 18 and 3 LST. However, the majority of HiRes evolutions show maximum precipitation at 21 LST. On the average the maximum precipitation of 20.9 ± 9.7 mm/day is observed at 21 LST (Figure 2a). When HiRes evolutions are time averaged to 6-hourly data, both an average of a spatial distribution during maximum precipitation (LoRes value) and its standard deviation are smaller (18.5 and 8.3 mm/day, respectively), while phase is well represented.

Over an ocean location (Figures 2c and 2d), the maximum precipitation rate is observed between 6 and 15 LST with value of about 4.7 mm/day and the standard deviation is 0.9 mm/day. At 15 LST the mean of all 100 HiRes evolutions is slightly higher (5.1 mm/day) and the standard deviation (1.4 mm/day) is substantially higher. This is due to a few grid boxes in which precipitation rates are substantially higher than in others, indicating effects of averaging over inhomogeneous topography (in this example due to location of Tanimbar Islands over Banda Sea). Comparison between spatial average of 100 HiRes evolutions and a single LoRes evolution shows good agreement, indicating that most of biases come from spatial averaging. The same conclusion can be reached when one considers HiRes temporal averaging only (Figure 2d). In this case 100 HiRes time series are time averaged to produce 100 individual 6-hourly evolutions. The average of these (that is LoRes evolution) and standard deviation at a given hour are consistent with mean and standard deviation of the original HiRes data. The largest discrepancies are observed for evolutions exhibiting a strong peak at 15 LST. This indicates that the primary source of bias in LoRes data is a result of spatial averaging. As a result, the rates of precipitation in LoRes data are smaller than in HiRes TRMM data in a number of locations/times. For example, the afternoon precipitation rate over Borneo has values of 15–17 mm/day in the HiRes data and 14 mm/day in the LoRes data. Caution must be used when analyzing data from coastal regions. As indicated in Figures 2c and 2d, even a marginal "contamination" of primarily oceanic grid box with land surface increases the standard deviation of the spatial distribution in this location. On the coasts of the islands, the contrast between land and ocean results in blending properties of the spatiotemporal characteristics of the diurnal cycle (Figure 1). It should also be noted that TRMM tends to underestimate the precipitation rate over steep topography (Matthews et al., 2013). Therefore, the TRMM precipitation rate over the islands should be considered a lower boundary estimate. This is especially true in low resolution.

This analysis shows that LoRes TRMM data are able to depict the most prominent spatial-temporal features of the diurnal cycle over the MC, but one needs to be cautious analyzing small-scale spatial features. Nevertheless, these data can be used to provide a benchmark for the GCM simulations of equivalent low resolution examined in the present study. However, this comparison is not a direct one, in that a LoRes TRMM point value is based on averaging data from higher resolution in space and time, while the corresponding point value from a GCM is based on a single estimate derived from the GCM, which includes errors both related to model parameterizations and coarse resolution.

2.3. Diurnal Cycle Metrics Derived From Precipitation Data

In order to assess the fidelity of GCMs in their representation of the complex temporal and spatial patterns of the diurnal cycle of precipitation over the MC, we focus on three variables derived from composite diurnal cycle of precipitation data following (Peatman et al., 2014): daily mean precipitation rate, amplitude, and phase of the diurnal cycle of precipitation. Let us consider the decomposition of the precipitation into its diurnal harmonic:

$$r = r_m\left\{1 + \frac{r_d}{r_m}\cos\left[\frac{2\pi}{T}(t - \phi_0)\right]\right\} \qquad A_r = \frac{r_d}{r_m} \tag{1}$$

where r is precipitation, r_m is its daily mean, r_d is amplitude of the diurnal cycle of precipitation, $T = 24$ h, t is hour of the day, and Φ_0 is hour of the phase (maximum of precipitation) of the diurnal cycle of precipitation. The ratio of the amplitude of the diurnal cycle of precipitation to the daily mean precipitation A_r is referred to

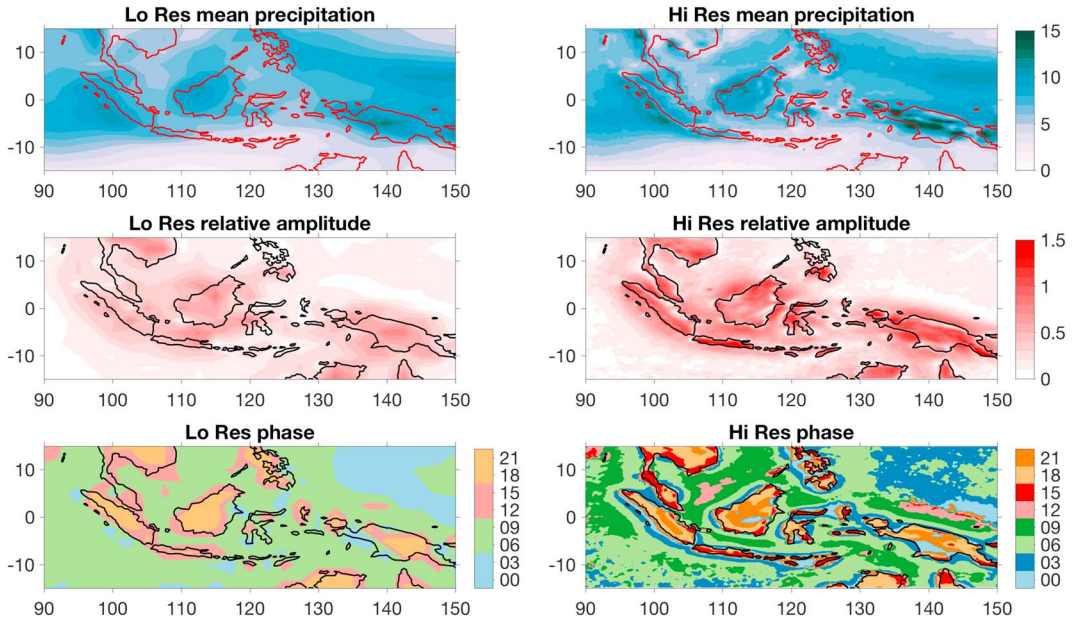

Figure 3. Daily mean precipitation rate (mm/day; top row), relative amplitude of the diurnal cycle (dimensionless, middle row), and phase of the diurnal cycle (LST hour; bottom row) calculated from (left column) low-resolution (LoRes) and (right column) high-resolution (HiRes) TRMM data.

here as the relative amplitude of the diurnal cycle of precipitation. This variable describes how big the diurnal cycle is relative to the mean precipitation and as such mitigates some of the mean precipitation biases between observational and modeling data sets to better distill the diurnal cycle amplitude. Hereafter, when we refer to the amplitude of the diurnal cycle of precipitation, we mean its relative amplitude A_r, unless otherwise indicated. The benefit of this approach (i.e., equation (1)) over other commonly used techniques, such as model data projection, is that it provides diurnal cycle metrics that are dependent solely on the given data set (observational or modeling) itself. All diurnal cycle metrics are calculated from the composite climatological diurnal cycle data, which means that first we calculate the mean diurnal evolution of the diurnal cycle for a given period (annual or seasonal mean) and then perform diurnal cycle decomposition.

2.3.1. The Daily Mean Precipitation Rate

Figure 3 shows the diurnal cycle metrics calculated from LoRes and HiRes TRMM data. The first row shows a comparison between the daily mean precipitation rates calculated from the two observational data sets. It can be seen that the spatial distribution is smoother and the daily mean precipitation rate is lower in LoRes TRMM data than in HiRes TRMM data. Over New Guinea the discrepancy between the two data sets is the largest—nearly 5 mm/day. Nevertheless, the spatial distribution of daily mean precipitation is generally well represented in LoRes data, including the local maxima of daily mean precipitation over the islands of New Guinea and Borneo, the maximum directly west of the west coast of Sumatra over the eastern Indian Ocean, and the maximum over the equatorial western Pacific. The clear minimum of daily mean precipitation over the ocean between the Indonesian islands and Australia is also well represented in LoRes TRMM data.

2.3.2. The Relative Amplitude and Phase of the Diurnal Cycle of Precipitation

The relative amplitude of the diurnal cycle (A_r in equation (1), hereafter A_r) indicates how strong the diurnal harmonic of precipitation is relative to the mean precipitation. For example, a value of 1 means that an amplitude of the diurnal harmonic is equal to the annual-average daily mean. The middle row in Figure 3 shows comparison between A_r calculated using LoRes and HiRes TRMM data, respectively. It can be seen that the MC region is characterized by higher diurnal cycle amplitude than either the eastern Indian Ocean or western Pacific Ocean. Within the region, the relative amplitude of the diurnal cycle is higher over land than over ocean. In the HiRes data, the relative amplitude of the diurnal cycle of precipitation over land achieves the value of 1 or exceeds it over all major islands. Within the MC region, maximum values of the relative

amplitude of the diurnal cycle exceeding 1.4 can be found over the islands of Java and Celebes. Most of the spatial variability of the relative amplitude of the diurnal cycle of precipitation, including higher values observed over land than over ocean, is exhibited in LoRes TRMM data although with a reduced amplitude. The poorest representations of amplitudes are for the local maxima over small islands such as Java and Celebes. This can be attributed to the low spatial resolution of the data set, which is too coarse to represent the fine-scale distribution over an island roughly the size of a grid point.

The phase of the diurnal cycle of precipitation (Φ_0 in equation (1), hereafter Φ_0) is defined by the hour of the maximum precipitation. Given known differences in convection development over land (Dai, 2001; Wallace, 1975) and over ocean (Chen & Houze, 1997; Gray & Jacobson, 1977), one can expect substantial spatial variability in phase of the diurnal cycle over the MC region. It has been shown that peak precipitation over land occurs during local afternoon, whereas over the ocean it occurs during the morning. This characteristic is well captured in Φ_0 derived from the HiRes TRMM data (bottom right panel in Figure 3). It can be seen that vast majority of land parts of the region show the hour of the maximum precipitation between 18 and 24 LST. Over Borneo, even the onset of precipitation along the coast (15–18 LST) and its inland propagation later during the day are represented at this high spatial and temporal scale. Over the ocean, precipitation is maximized between 00 and 12 LST. Progression of the precipitation maximum west of the coast of Sumatra and northeast of the coast of New Guinea is clearly visible. In fact northeastward propagation of the precipitation off the northeastern coast of New Guinea can be tracked for 24 hr using annually averaged data presented here. Much of the fine-scale details of the phase of the diurnal cycle are lost in the LoRes TRMM data (bottom left panel in Figure 3). However, the clear difference in phase of the diurnal cycle can still be seen over Sumatra, Borneo, New Guinea, and surrounding seas. Such a change can be attributed in part to the decreased (by half) number of phases. Instead of eight distinct phases in HiRes TRMM, the LoRes TRMM data has only four phases that can be assigned. One should note that in reality the difference in precipitation evolution over land and ocean is more complex than a simple shift in maximum (Chen & Houze, 1997; Gray & Jacobson, 1977). It can be assessed by examining higher statistical moments of diurnal precipitation distribution (skewness and kurtosis), which reflect asymmetry in convection development between land and ocean. Thus, decomposition of the diurnal cycle into a single harmonic does not allow full assessment of differences between evolution over land and ocean. However, the temporal scale of those differences (a few hours; after Chen & Houze, 1997) is below the temporal resolution of HiRes and especially LoRes data. Thus, asymmetry in convection development, although relevant, cannot be assessed using data available to this study.

2.3.3. Effects of Spatial and Temporal Averaging on Diurnal Cycle Characteristics

It has been shown above that LoRes TRMM data well represent the diurnal evolution of precipitation, although underestimation of the amplitude of the diurnal cycle resulting from both temporal and spatial averaging is apparent (Figures 2 and 3). Figure 4 presents a comparison between diurnal cycle metrics (mean precipitation, amplitude, and phase of the diurnal cycle) calculated for a two LoRes grid box regions over MC (New Guinea and Banda Sea). It can be seen that temporal averaging has no effect on the mean precipitation. Spatial averaging of the HiRes data provides an estimate of the daily mean precipitation of 10.7 ± 3.1 mm/day in New Guinea (Figure 4a) and 4.1 ± 0.5 mm/day in Banda Sea (Figure 4b) example. These estimates are the same as estimates calculated using data averaged to 6-hourly (temporal averaging) and match the LoRes estimate (spatial and temporal averaging).

The relative amplitude of the diurnal cycle (dimensionless) shows a bias when data are time averaged, resulting in about 15% underestimation of its magnitude (Figures 4b and 4e). The spatial distribution of the original HiRes data over New Guinea has an average of 1.10 with standard deviation of 0.02. Over the Banda Sea values are lower, with an average 0.17 and standard deviation of 0.05. Time averaging the data to four points per day results in an average value of 0.95 ± 0.21 over New Guinea and 0.26 ± 0.09 over Banda Sea. The LoRes TRMM data (single evolution) have average values of 0.78 and 0.21 over New Guinea and Banda Sea, respectively.

The spatial distribution of the phase of the diurnal cycle is consistent between data sets (Figures 4c and 4f). Over New Guinea the HiRes data provide an estimate of 21.44 ± 2.11 LST, time-averaged data give 21.44 ± 2.03 LST, and the LoRes data estimate is 21.67 LST. Over Banda Sea the original HiRes data give a phase estimate of 10.06 ± 1.46 LST; in time-averaged data the phase is 10.18 ± 1.68 LST and the value for LoRes data is 10.22 LST.

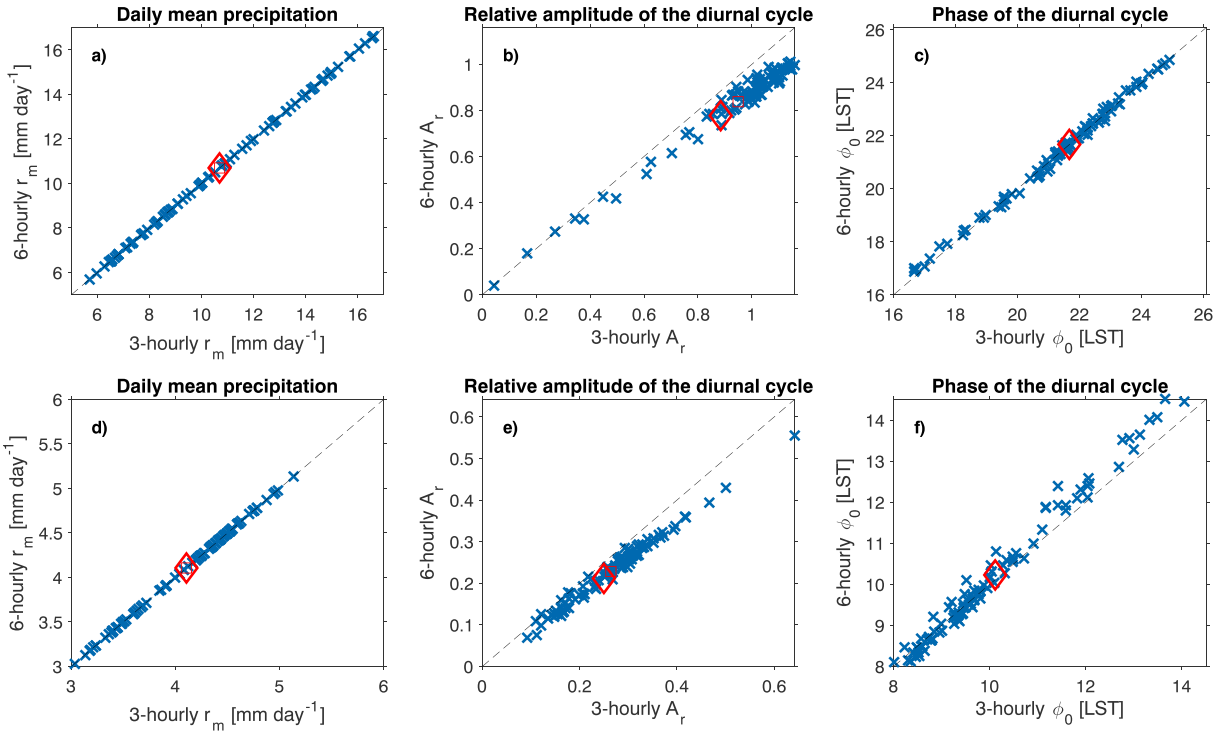

Figure 4. Comparison between diurnal cycle characteristics calculated using low-resolution and high-resolution TRMM mean diurnal cycle data for a reference location at New Guinea(142.5°E and 5°S; a–c) and Banda Sea (130°E and 7.5°S; d–f). Panels show daily mean precipitation (a, d), relative amplitude of the diurnal cycle (b, e), and phase of the diurnal cycle (c, f). In each panel, *x* axis represents original 3-hourly data; *y* axis shows 6-hourly data. Blue crosses show comparison between original HiRes data and data averaged in temporal dimension only. Red diamond shows comparison between low-resolution TRMM value and value of the high-resolution data averaged in spatial dimension only.

These estimates show that uncertainty of the LoRes estimate of diurnal cycle metrics is dominated by spatial averaging, which is consistent with Figure 2. They indicate that temporal variability of the diurnal cycle is represented in LoRes data but the spatial variability associated with local (subgrid-size) conditions is clearly diminished.

2.3.4. *AmPm* Index

Because the spatial distribution of the phase of the diurnal cycle is associated with the distribution of land and ocean within the MC region, a metric that exhibits this variability simply can be derived. Here we are mainly interested in the zonal variability of the diurnal phase, because the MC region is bounded by two oceans that are clearly characterized by nighttime precipitation maxima. This new metric (hereafter *AmPm* index) utilizes the difference in the hour of the precipitation maxima between land and ocean. It represents a deficit or excess of local solar time morning precipitation over afternoon precipitation. The deficit largely characterizes land regions and the excess is typical for ocean regions. The new *AmPm* index is defined as follows:

$$AmPm = \frac{r_{AM} - r_{PM}}{r_{AM} + r_{PM}} \tag{2}$$

where r_{AM} and r_{PM} refer to the local solar time morning (a.m.; 03–14 LST) and local solar time afternoon (p.m.; 15–02 LST) components of the precipitation, respectively. The 3-hr shift relative to local noon/midnight is due to the typical persistence of convection, which persists over land into next day early morning and over ocean into early afternoon (Baranowski et al., 2016). However, we refer to these two distinct temporal bins as morning and afternoon to highlight the canonical difference in the phase of the diurnal cycle between land and ocean.

Note that since the denominator in equation (2) is always positive, if the morning component dominates over the afternoon one, the *AmPm* is positive. If the afternoon component is larger than morning component, the

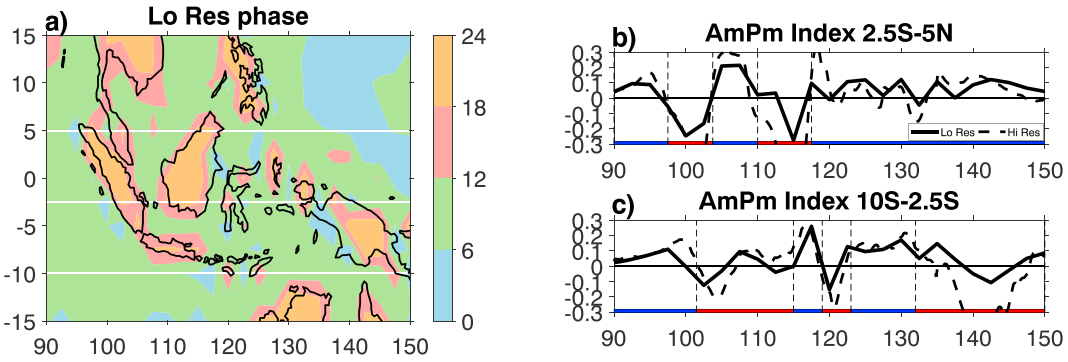

Figure 5. Map of the phase of the diurnal cycle (LST hour) derived from (a) LoRes TRMM data and zonal distribution of the *AmPm* index (right) averaged between 2.5°S and 5°N (b), and 10°S and 2.5°S (c), derived from both LoRes (solid) and HiRes (dashed) TRMM data. White lines indicate meridional bands used for *AmPm* index calculation. Blue and red shading indicate ocean and land within the Maritime Continent region. LoRes = low-resolution; HiRes = high-resolution.

AmPm has a negative value. The magnitude of the index indicates the relative difference between the two components: the greater the difference, larger the absolute value of the *AmPm* index. In the extreme cases, if the precipitation were solely morning or afternoon, the index would have an absolute value of 1.

In this study we calculate the *AmPm* index from precipitation data averaged in two bands: around the equator between latitudes 2.5°S and 5°N (to highlight variability between Sumatra, Borneo and adjacent seas) and between latitudes 10°S and 2.5°S (to highlight variability between New Guinea and adjacent seas). Zonal cross section along the MC region over these meridional bands is characterized by the largest variability between ocean and land surfaces (Figure 5a). It can be seen (Figures 5b and 5c) that the *AmPm* index represents the zonal distribution of land and oceans very well and simplifies the more complex map of the distribution of the phase of the diurnal cycle. The comparison between *AmPm* indices calculated using LoRes and HiRes TRMM data shows a high correlation, which confirms that differences in diurnal cycle characteristics between land and ocean can be well depicted at the coarse resolution of the models' output. The zonal progression of the *AmPm* index is such that it has a positive value over the Indian Ocean and increases as one approaches the coast of Sumatra, as a result of a strong and coherent diurnal cycle of precipitation (Figure 3). The values of the index calculated in the equatorial band (2.5°S to 5°N) over Sumatra (100–103°E) and over Borneo (110–118°E) are negative, whereas it is positive over the sea between them; over the western Pacific (east of 135°E), the *AmPm* index becomes positive again. In the southern band (10–2.5°S), values are positive west of 100°E (Indian Ocean) and become negative at longitudes of the southern part of Sumatra and Java islands (100–107°E), Celebes (119–123°E) and New Guinea (132–148°E); index assumes positive value over seas surrounding the islands (Java Sea and Banda Sea). These zonal variations of the *AmPm* index are clear reflections of the varying characteristics of the diurnal distribution of precipitation between land and ocean, suggesting that the *AmPm* index is a simple, relatively intuitive, metric that readily illustrates the nature of the diurnal cycle in precipitation in the MC region. Since the zonal variability of the *AmPm* index across the MC is well represented in the LoRes TRMM data, it can be easily utilized in our model performance assessment.

3. Mean Precipitation and Mean Diurnal Cycle of Precipitation

The precipitation metrics described above are utilized in this section along with the LoRes TRMM data to assess the performance of GASS/MJOTF models in representing the diurnal cycle of precipitation. We begin by looking at the annual mean of the daily mean precipitation, followed by the relative amplitude (A_r) and phase of the diurnal cycle (Φ_0). A bias, which we refer to in this section, is defined as model value minus reference data set (LoRes TRMM) value.

3.1. Daily Mean Precipitation

Figure 6 illustrates the bias of the mean rainfall pattern simulated by the GCMs relative to the LoRes TRMM data defined as a difference between model and TRMM data. Note that mean rainfall patterns for the

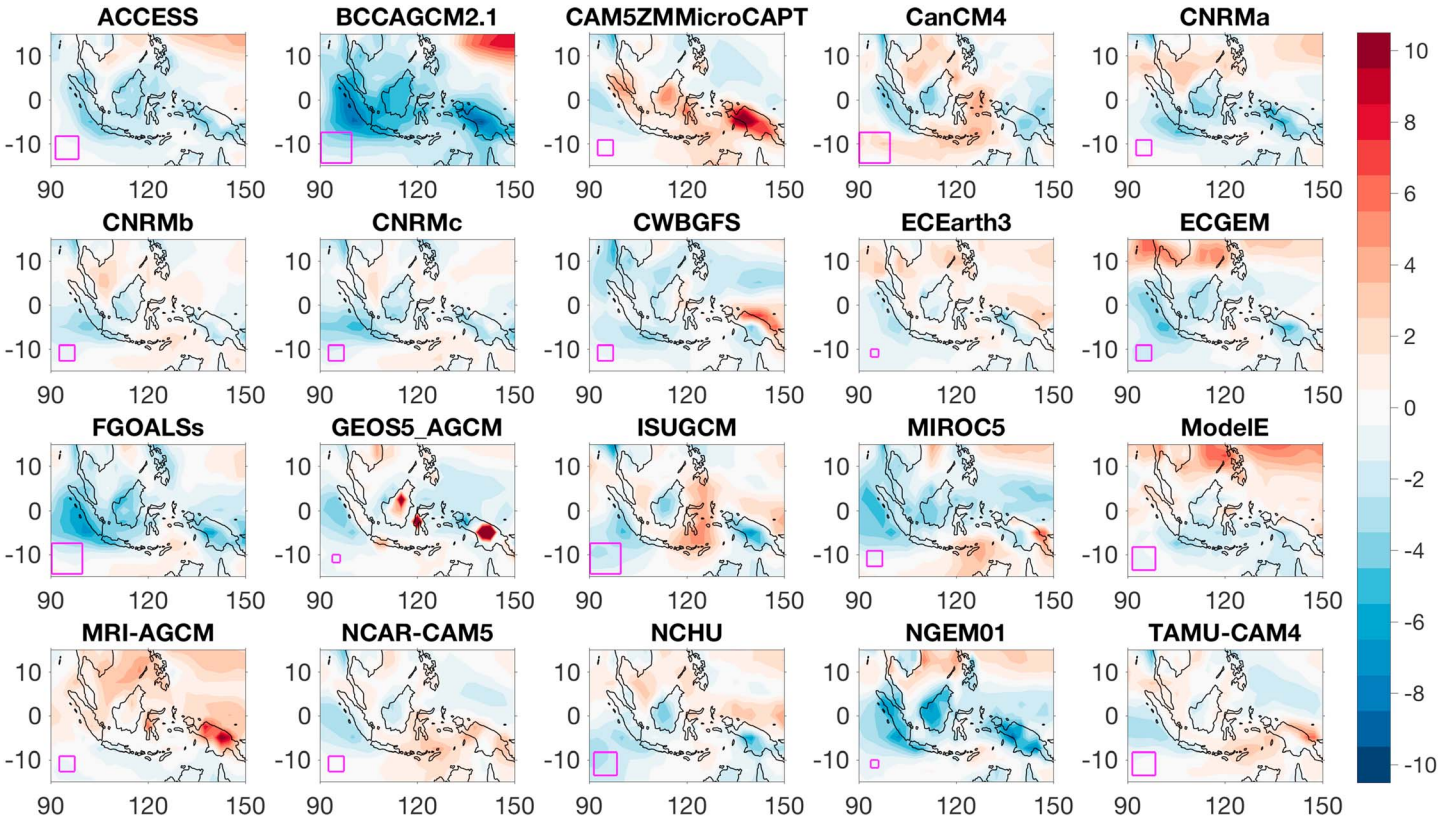

Figure 6. Daily mean precipitation rate bias (mm/day). Each panel is a map for one GASS/MJOTF model (see color bar for shading legend and Table 1 for model names and details). Magenta markers in bottom left corner indicate model's native resolution; models are divided into four bins: 0–100 (smallest squares), 100–200, 200–300, and above 300 km (largest squares).

models are derived from the full 20-year-long climate simulations, whereas the observation reference is based on TRMM, using a 15-year-long period, from 1998 to 2013. However, sensitivity tests conducted off-line show that mean and variability statistics derived from models' precipitation data are not qualitatively dependent on whether we use a 15- or 20-year assessment period.

It is evident that the models have various biases in the mean precipitation pattern over the MC region. A few systematic biases can be identified across these models. For example, all but one model (MRI-AGCM) show a negative bias over the eastern Indian Ocean. Additional systematic biases tend to occur in two groups. The first group of models, including ACCESS, BCCAGCM2.1, CNRMa, CWBGFS, ECGEM, FGOALSs, MIROC5, and NGEM01, shows negative daily mean precipitation biases over most of the MC region. Although CNRMc, ECGEM, and FGOALSs show slight positive biases (less than 0.7 mm/day) over the Banda Sea and MIROC5 shows positive biases exclusively over the Banda sea (26%) and New Guinea (5%), these models are included in the same group as they show negative biases over other parts of the MC region. Among the models in the first group, the bias is the largest in BCCAGCM2.1, exceeding 50% (i.e., more than 6 mm/day over eastern Indian Ocean, Sumatra, and New Guinea) over all land and ocean regions within the MC. Within this group of models, only CWBGFS shows a larger bias over ocean than over land. All other models in this group show a larger negative bias over land than over ocean. For example, the NGEM01 model shows a large negative bias (exceeding 70% or 5 mm/day) over land, a strong negative bias over the eastern Indian Ocean (35% or 3.5 mm/day) and a relatively small bias (less than 6%) over the seas within the MC region. This bias pattern is the most common and is consistent with the multimodel ensemble mean bias (not shown).

The second group of models exhibits a negative bias over land and a positive bias over the seas. This group includes models such as CanCM4, CNRMb, CNRMc, ECEarth3, ISUGCM, NCAR_CAM5, NCHU, and TAMU-CAM4. Among these models, the smallest bias over land and ocean is seen in the ECEarth3 GCM (less than 15%). All models, whether from the first or the second group, exhibit bias patterns

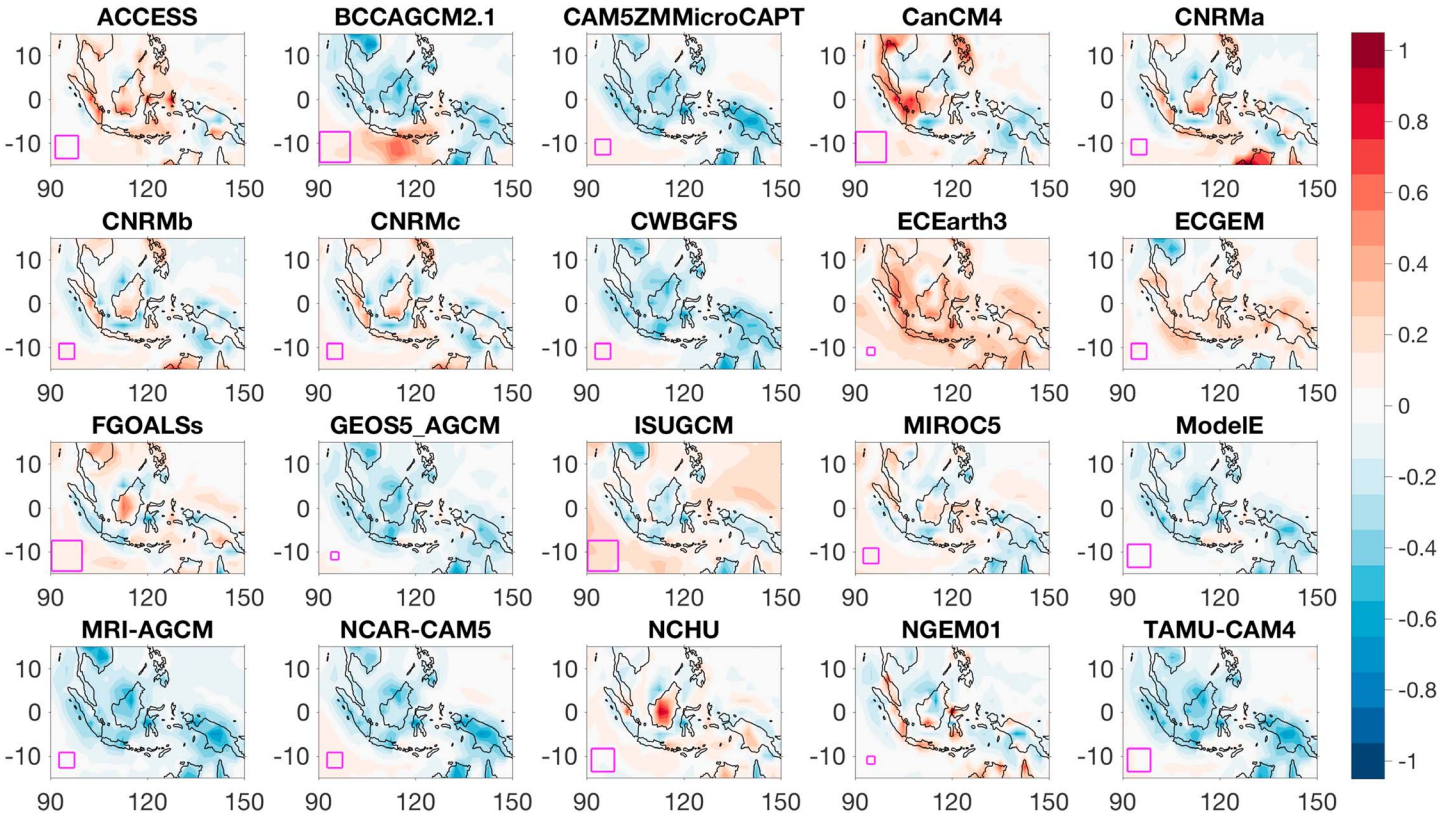

Figure 7. Relative amplitude of the diurnal cycle of precipitation bias (dimensionless). Each panel is a map for one GASS/MJOTF model (see color bar for shading legend and Table 1 for model names and details). Magenta markers in bottom left corner indicate model's native resolution; models are divided into four bins: 0–100 km (smallest squares), 100–200, 200–300, and above 300 km (largest squares).

that result in a decrease in the land-sea contrast of the mean precipitation. Observations (Figure 3) clearly show that precipitation is higher over the islands within the MC than over adjacent seas (with the exception of the equatorial Indian Ocean west of Sumatra).

Interestingly, there is some variability within the CNRM family. The atmosphere-only (CNRMa) realization shows mostly negative bias south of 5°N and positive bias over the South China Sea, western Pacific, and Indian Ocean north of 5°N. This means that the bias is negative above major islands and surrounding seas. In the coupled version (CNRMb), the positive bias in the northern part of the region is reduced. The negative bias over the eastern Indian Ocean is also slightly reduced and so is the negative bias over land. The seas within the MC region are characterized by small positive bias in the coupled simulation. Overall, the coupled simulation shows a mean precipitation pattern closer to the observations. The CNRMc run exhibits a pattern and bias structure similar to the coupled CNRMb simulation. This indicates that a correct state of the ocean is more important than coupling itself as it may reduce mean precipitation biases over the MC region. However, bias patterns from all of the CNRM simulations tend to reduce the land-sea contrast in the mean precipitation over the MC.

Two models (CAM5ZMMicroCAPT and GEOS5_AGCM) clearly increase the land-ocean contrast in mean precipitation exemplified by strong positive biases over land (especially New Guinea) and smaller or even negative biases over the seas. The MRI-AGCM model also shows a strong positive bias over New Guinea, but this model (and ModelE) shows a clear meridional gradient—positive bias dominates north of the equator and negative in the southern part of the MC region.

Interestingly, three models, which were run in the finest native spatial resolution (less than 100 km), are scattered across three groups summarized above. This confirms that model's resolution should not be considered a sole benchmark for fidelity in representation of the mean precipitation pattern over the MC region.

3.2. Relative Amplitude of the Diurnal Cycle

Similar to biases in the mean precipitation, many models exhibit coherent biases with respect to A_r, namely, in underestimating it over the entire MC region, especially over land (Figure 7). Such a feature is characteristic of 8 out of 20 models (BCCAGCM2.1, CAM5ZMMicroCAPT, CWBGFS, GEOS5_AGCM, ModelE, MRI-AGCM, NCAR-CAM5, and TAMU-CAM4), which span the spectrum of native spatial resolution represented in the models examined here. It should be noted that negative bias may result from overestimation of the daily mean precipitation (e.g., MRI-AGCM). The bias over land is of the order of 0.3–0.7 and over ocean 0.1–0.2. Because the observed A_r in the MC region is larger over land than over ocean (Figure 3), the abovementioned models decrease the land-sea difference and produce a weaker and more spatially uniformly pattern of the diurnal cycle relative amplitude. It should be noted that the CAM5ZMMicroCAPT and GEOS5_AGCM models increase the land-sea contrast with respect to the daily mean precipitation and this increase contributes to the decreased contrast in the relative amplitude. The ECGEM model exhibits a positive bias over much of the MC region, but the bias is larger over ocean than over land. This means that this GCM also decreases the land-ocean contrast.

A second group of models, ACCESS, FGOALSs, MIROC5, NCHU, and the CNRM family models, increase the land-sea contrast in the A_r. Some of these models increase the diurnal cycle amplitude over land while decreasing it over ocean (CNRM models, FGOALSs, and NCHU); others increase it across entire region, but the increase over islands is larger than over adjacent seas (ACCESS and MIROC5). In both cases, the result is to increase the relative difference in the A_r between the land and ocean parts of the MC region. It can be seen that there are virtually no differences in the pattern of the relative amplitude bias within the CNRM family. Models, which belong to this group, were run in intermediate (100–300 km) resolutions; none of the highest ($<$100 km) or the coarsest ($>$300 km) native resolution models can be found here.

Specific features of the biases in two other models stand out: ECEarth3 and ISUGCM. The first fits into the second group discussed above because it increases land-sea contrast, but it is also unique as it increases the magnitude of the diurnal cycle over almost the entire domain. The second of the models has a positive bias over the Indian Ocean and western Pacific and negative bias over the MC region and Southeast Asia. The negative bias is larger over islands than over adjacent seas. In fact, the full (not relative) diurnal cycle amplitude (not shown) shows that ISUGCM model barely "sees" the MC region with respect to this metric; that is, the diurnal variation of precipitation is only a little smaller over islands than over ocean regions.

The NGEM01 model exhibits biases in A_r with extraordinary spatial variability, especially along the coastlines. For example, over Borneo and New Guinea both positive and negative biases are visible. This feature is unique among GASS/MJOTF models and is likely due to the fact that this model has the highest native spatial resolution. Another outlier is the CanCM4 model, which shows some features similar to the models that decrease the land-sea contrast in A_r. For example, it shows a slight positive bias over the Indian Ocean and western Pacific and negative bias over much of the MC region. However, it also shows a strong positive bias over Southeast Asia and the Malay Peninsula, which extends to Sumatra and the southern part of the South China Sea.

The multimodel ensemble mean bias (not shown) pattern and magnitude shows little resemblance to any of the abovementioned groups. This is because negative (positive) biases of some models are mitigated by positive (negative) biases of others, a consequence of the fact that there is little agreement among the investigated GCMs with respect to A_r over the MC region.

3.3. The Phase of the Diurnal Cycle

Figure 8 shows maps of Φ_0 for the various model simulations. Note that it presents actual phases calculated from each model's precipitation data, not biases. Therefore, each map should be compared with the LoRes TRMM phase of the diurnal cycle (Figure 5) for reference.

It can be seen that many models exhibit a change in Φ_0 caused by islands within the MC. Two models—BCCAGCM2.1 and ISUGCM—shows only marginal land-ocean difference in relation to the phase of the diurnal cycle. The difference in the peak hour of precipitation between land and ocean regions is only 6 hr, but models do not agree even with each other on the timing. ISUGCM produces maximum precipitation over

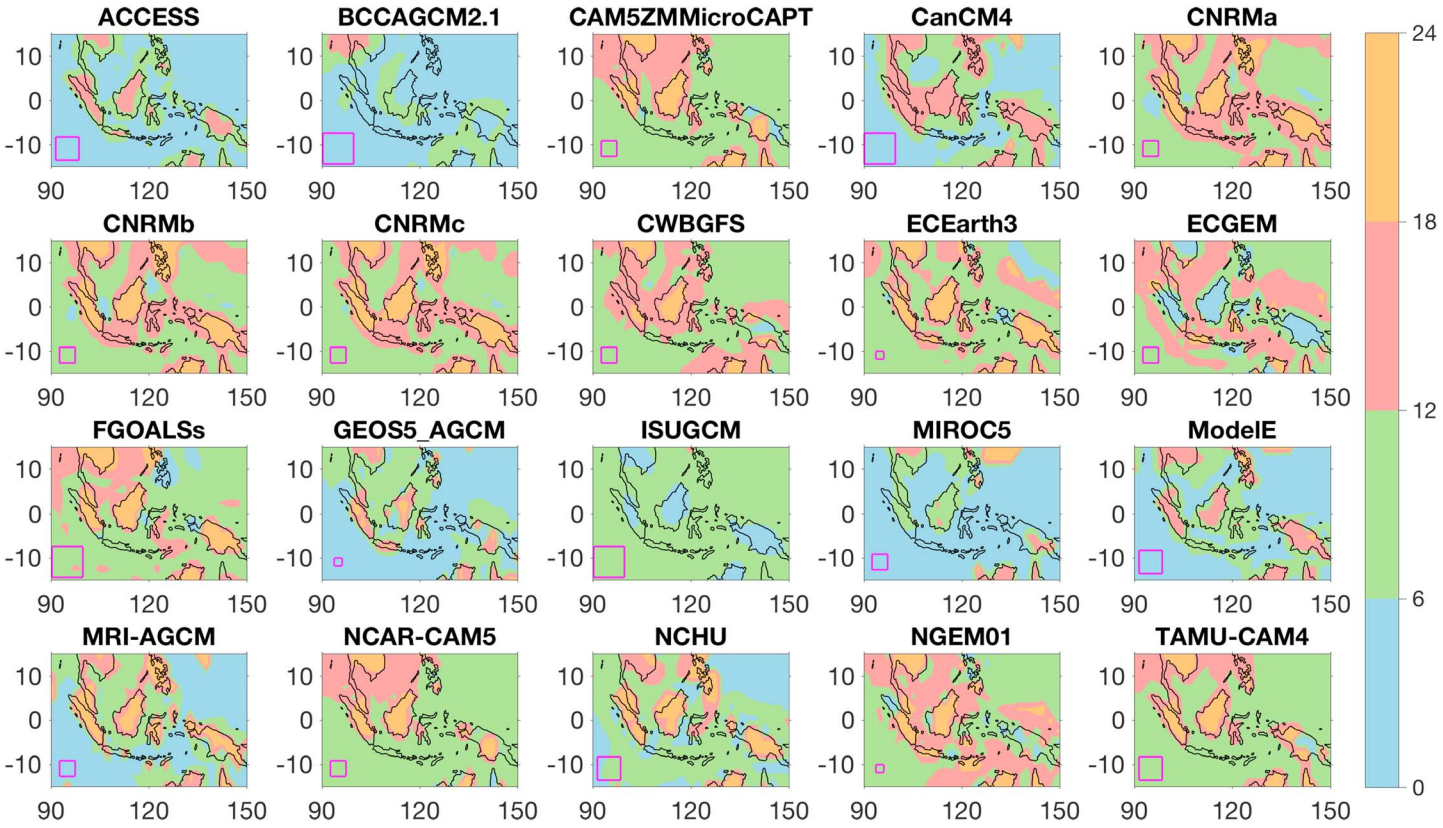

Figure 8. Maps of the phase of the diurnal cycle of precipitation (LST hour). Each panel represents one GASS/MJOTF model (see color bar for shading legend and Table 1 for model names and details). Magenta markers in bottom left corner indicate model's native resolution; models are divided into four bins: 0–100 km (smallest squares), 100–200, 200–300, and above 300 km (largest squares).

land during 0–6 LST and precipitation over ocean 6 hr later. The spatial distribution of maximum precipitation in BCCAGCM2.1 is a modestly modulated by islands within the MC region, but it occurs in the vicinity of the islands 6 hr after the maximum over ocean (0–6 LST). Furthermore, this model shows a bias in the phase of the diurnal cycle of precipitation over the Indian Ocean, where it peaks too early in comparison with observations. These are two of the models run with the coarsest resolution (>300 km).

Other models perform better in this respect, showing a spatial distribution of the phase strongly consistent with the land-sea mask. A few systematic biases emerge when considering the performance of this collection of models. The first group exhibits a pattern, which closely matches the observations, having not only a clear phase difference between the MC islands and surrounding oceans but in which the actual phases over both land and ocean are consistent with observations, including a 12-hr phase difference between them. This first group includes the CAM5ZMMicroCAPT, CNRM family, CWBGFS, ECEarth3, FGOALSs, NCAR-CAM5, NCHU, NGEM01, and TAMU-CAM4 models. Models in this group tend to produce precipitation over open ocean and Banda Sea during 06–12 LST and over major islands during 18–24 LST. Their performance varies with respect to the phase of the diurnal cycle around Borneo (South China Sea, Karimata Strait, and Java Sea), which may relate to differences in their native resolutions and common grid resolution. The latter requires blending between ocean and land like diurnal cycle in the coastal regions (Figures 2 and 4).

A second group exhibits a pattern similar to the first one, with the difference that maximum precipitation over Indian Ocean occurs about 6 hr too early (00–06 LST). Such behavior is characteristic of ACCESS, CanCM4, MIROC5, and ModelE, which show a peak in precipitation over land 6 hr (MIROC5) or 12 hr (all others) after the maximum precipitation occurred over ocean. GEOS5_AGCM and MRI_AGCM also show a peak in precipitation over the Indian Ocean too early, but their peak in precipitation over land is consistent with observations.

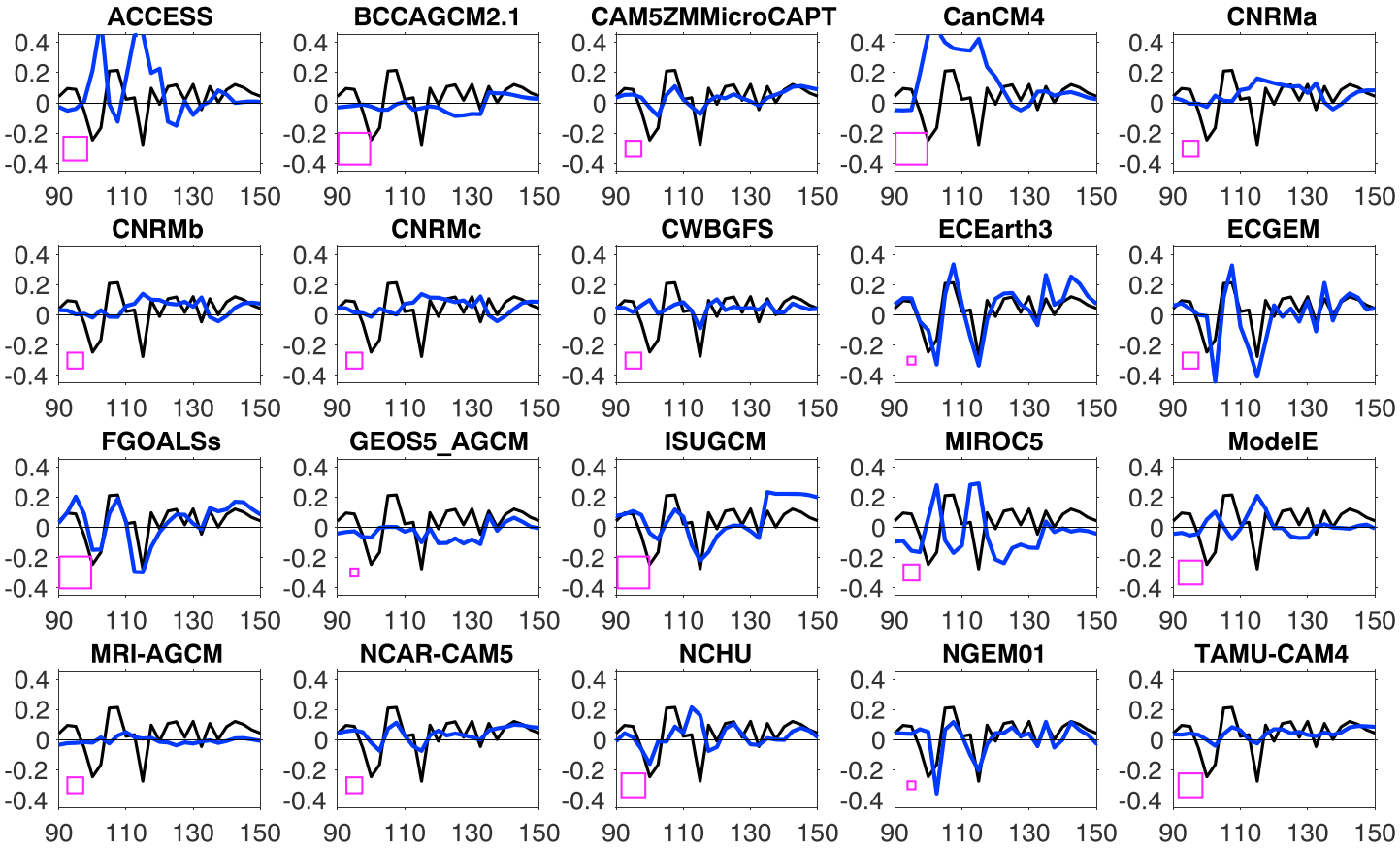

Figure 9. Zonal distribution of *AmPm* index for GASS/MJOTF models and observations. On each panel the blue line represents a model and black line represents low-resolution TRMM observations. Magenta markers in bottom left corner indicate model's native resolution; models are divided into four bins: 0–100 (smallest squares), 100–200, 200–300, and above 300 km (largest squares). Presented *AmPm* index is calculated in 2.5°S to 5°N meridional band.

Finally, the ECGEM model shows the correct phase of the diurnal cycle over open ocean (06–12 LST), but the peak of the precipitation over land occurs consistently too late into the night in comparison with observations (00–06 LST). Furthermore, it shows clear regions affected by both regimes and blended due to spatial averaging.

Figure 9 shows the zonal variability of the *AmPm* index calculated from each model's precipitation data. Because the index is sensitive to the difference in the local solar time morning and afternoon precipitation, it shows whether a model correctly simulates the timing of precipitation across the MC domain. We use two bands for calculating *AmPm* index, consistent with Figure 5 but plot *AmPm* for equatorial band only. Values of the *AmPm* index score, defined as correlation between model's and observed section, can be found in Table 2. It can be seen that CAM5ZMMicroCAPT, CWBGFS, ECEarth3, ECGEM, FGOALSs, ISUGCM, NCAR-CAM5, NCHU, NGEM01, and TAMU-CAM4 correctly simulate the zonal variations of the excess/deficit of local solar time morning over afternoon precipitation. Most of these models belong to the first group highlighted above, which simulated a realistic spatial distribution of the phase of the diurnal cycle and ECGEM produces precipitation over land consistently at the correct phase (Figure 8). Within this group of models, a subgroup consisting of CAM5ZMMicroCAPT, ECEarth3, ECGEM FGOALSs, and NGEM01 can be identified. These models not only show a correct zonal distribution of positive and negative values of the *AmPm* index, but their zonal distribution closely follows the observed one in both bands, indicated by variability consistent with observation in the equatorial band (Figure 9) and *AmPm* index score above 0.5 in both bands (Table 2). This suggests that these models not only simulate the correct phase but also more realistically simulate the diurnal cycle amplitude and its zonal variability. In fact, these models tend to

Table 2
AmPm Index Score Calculated as Correlation Between GASS Model AmPm Index Correlation With LoRes TRMM Data Over MC region (90–150°E)

Model name	*AmPm* index score (2.5°S to 5°N; 90–150°E)	*AmPm* index score (10–2.5°S; 90–150°E)
ACCESS	−0.70	−0.73
BCCAGCM2.1	0.14	−0.13
CAM5ZMMicroCAPT	0.74	0.60
CanCM4	−0.45	−0.37
CNRMa	−0.13	0.19
CNRMb	−0.22	0.17
CNRMc	−0.15	0.18
CWBGFS	0.35	0.30
ECEarth3	0.82	0.65
ECGEM	0.72	0.55
FGOALSs	0.68	0.59
GEOS5_AGCM	0.42	0.06
ISUGCM	0.48	0.08
MIROC5	−0.55	−0.42
ModelE	−0.60	−0.22
MRI-AGCM	−0.06	−0.37
NCAR-CAM5	0.74	0.53
NCHU	0.19	0.32
NGEM01	0.63	0.23
TAMU-CAM4	0.68	0.39

Note. AmPm index is calculated for two meridional bands: 2.5°S to 5°N (middle column) and 10–2.5°S (right column).

overestimate land-sea contrast in the diurnal cycle amplitude (Figure 7). NGEM01 and TAMU-CAM4 also show good performance in then equatorial band (>0.6), but it drops significantly in the southern band, dominated by performance over Banda Sea and New Guinea. These models simulate the phase of the diurnal cycle relatively well, but with a smaller daily mean precipitation (NGEM01) or smaller relative amplitude of the diurnal cycle (TAMU-CAM4).

A second group of models, ACCESS, ModelE, and MIROC5, exhibit zonal variability, which is reversed in comparison with observation, namely, the *AmPm* index is positive over land and negative over ocean, which is opposite from observations. This is consistent with analysis of the phase of the diurnal cycle.

The rest of the models show either little zonal variability in the phase of the diurnal cycle or values of Φ_0 that are not correlated with land and ocean across the MC region. In this category we find both the model, which shows no spatial variability of the phase of the diurnal cycle (BCCAG CM2.1) as well as models for which the phase of the diurnal cycle is off by 6 hr. The latter models are able to represent the spatial variability of the phase of the diurnal cycle consistent with the distribution of land and ocean within the MC region, but due to too early and/or too late precipitation peaks, they blend the local solar time a.m. and p.m. distinction between ocean and land precipitation maxima.

3.4. Regional Characteristics and Consolidated Performance Measures

The evaluation of the diurnal cycle of precipitation in the models illustrates a number of systematic biases with considerable differences between the models and regional dependencies. In particular, many models exhibit a strong dependence in their bias characteristics on the distribution of land and ocean in the region. We will more closely examine such features by focusing on six distinct subregions within the MC: three land regions (Sumatra, Borneo, and New Guinea) and three ocean regions (eastern Indian Ocean, seas around Borneo, and Banda Sea). Sumatra and eastern Indian Ocean regions are represented by 7, New Guinea by 9, Borneo by 10, Banda Sea by 11, and seas around Borneo by 26 LoRes grid points. A small map showing these regions is provided in the figures evaluating regional characteristics (Figures 10–13).

Figure 10 presents the consolidated model performance with respect to the key metrics presented above over the six regions. For composite diagrams, daily mean precipitation (normalized by observations) is illustrated with the size of the symbol (see legend), relative diurnal cycle amplitude (A_r) is illustrated via the radial distance from the origin, and phase (Φ_0) is illustrated via the angle with respect to the horizontal, with each of the four distinct phases possible annotated in terms of their local time. Ocean (land) regions are given on the left (right) column of the figures. Observations (black crosses) confirm that A_r is higher over land regions (0.4–0.5) than over ocean regions (less than 0.4). The difference in the hour of the maximum precipitation (Φ_0) between islands and surrounding oceans is apparent. The difference in phase of the diurnal cycle between neighboring ocean and land regions is always about 12 hr. It can be seen that models tend to underestimate A_r over ocean regions (i.e., most symbols lie closer to the origin than the X symbol for the observations). Only six models (ACCESS, CanCM4, ECEarth3, ECGEM, FGOALSs, and ISUGCM) simulate A_r of similar magnitude to the observation (distance from the origin of those models markers similar to the observations marked by the X symbol) over ocean regions. ISUGCM consistently shows the A_r slightly higher than observed. Over land regions, GCMs show larger scatter in A_r. Although most models underestimate this metric, about 40% of them show A_r higher than observations.

With respect to the mean precipitation (i.e., size of the marker), all but one model shows a negative bias over the eastern Indian Ocean region (i.e., most are diamonds or small circles, and not squares or big circles). Over land, some models overestimate while others underestimate the mean precipitation.

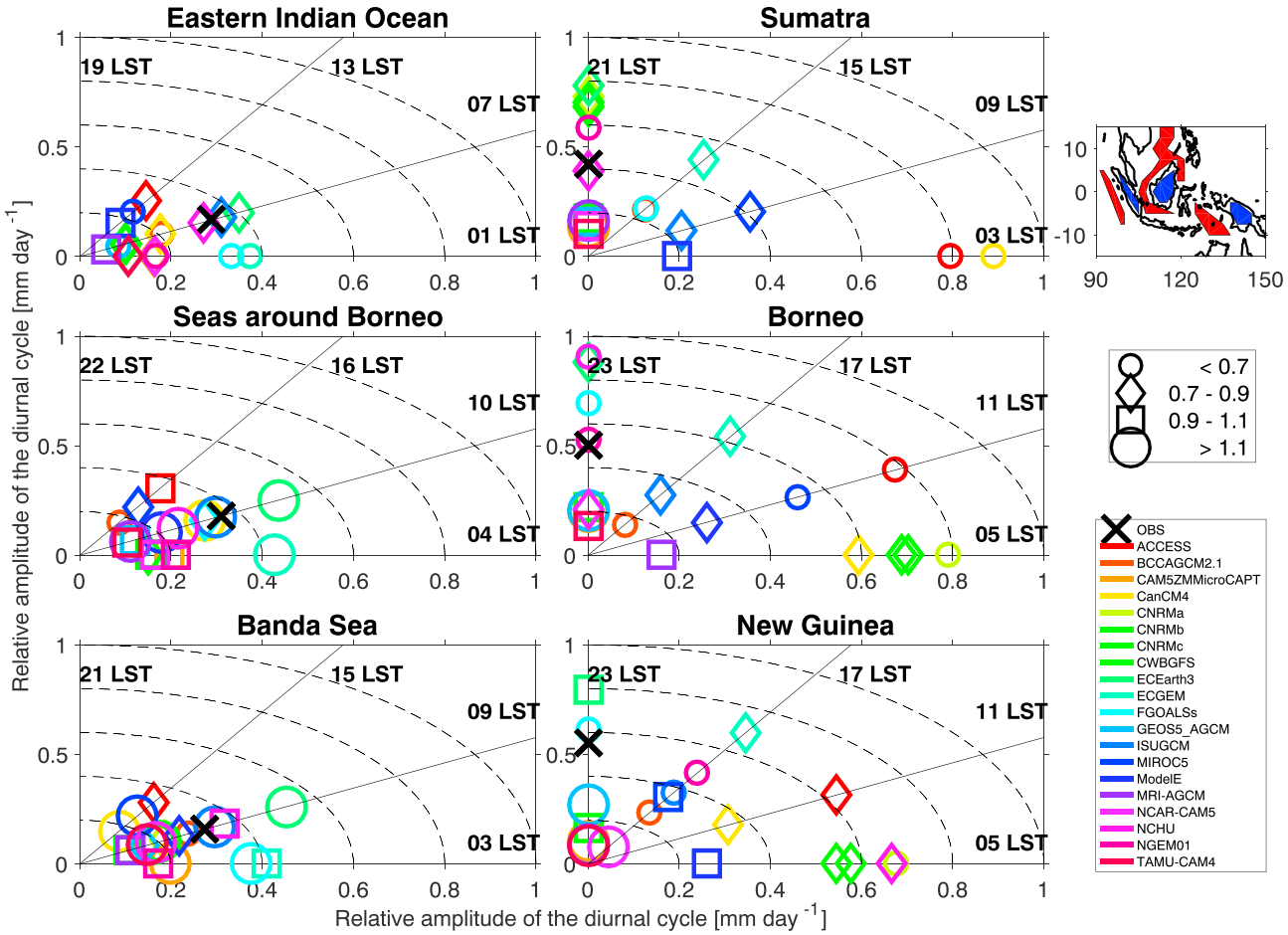

Figure 10. Regional performance of the GASS/MJOTF models with respect to the mean precipitation (size and shape of a marker) normalized by observations, relative amplitude of the diurnal cycle (radial distance from [0,0]) and phase of the diurnal cycle (angle). Each panel represents models' performance over one region. Observations are marked with thick black cross. The map in the upper right shows all ocean (red) and land (blue) regions analyzed in the figure.

This regional assessment finds that models tend to perform better with respect to the phase and amplitude of the diurnal cycle over ocean than over land within the MC region. However, over all regions at least 40% of models correctly simulate the time of the precipitation maximum. Model performance with respect to Φ_0 is the worst over the land regions of Borneo and New Guinea, where only 60% of them simulate the local afternoon precipitation peak. This means that over those regions 40% of models show precipitation maxima during the local solar time morning (a.m.), which is typical for ocean, not land regions. Furthermore, over land regions models that overestimate the daily mean precipitation (i.e., big circle markers) vastly (by 50% or more) underestimate A_r. This means that the contribution of the diurnal cycle to the daily mean precipitation over land is too small in these models, indicating that the daily mean precipitation is in fact unrealistically enhanced. Over ocean regions (i.e., the Banda Sea and seas around Borneo) models that overestimate the daily mean precipitation show both increased and decreased A_r in comparison with observations.

4. Seasonal Cycle of Precipitation and Diurnal Cycle of Precipitation

So far we have shown how the GASS/MJOTF models perform with respect to the annual mean of the daily mean precipitation rate, diurnal cycle amplitude, and phase. Here the seasonal cycle of these key metrics will be explored. We will again employ regional assessment and focus on the previously defined six regions.

Figure 11 presents the seasonal cycle of the daily mean precipitation rate for observations and models, defined as a 3-monthly anomaly. It can be seen that all regions have some seasonal cycle of the daily

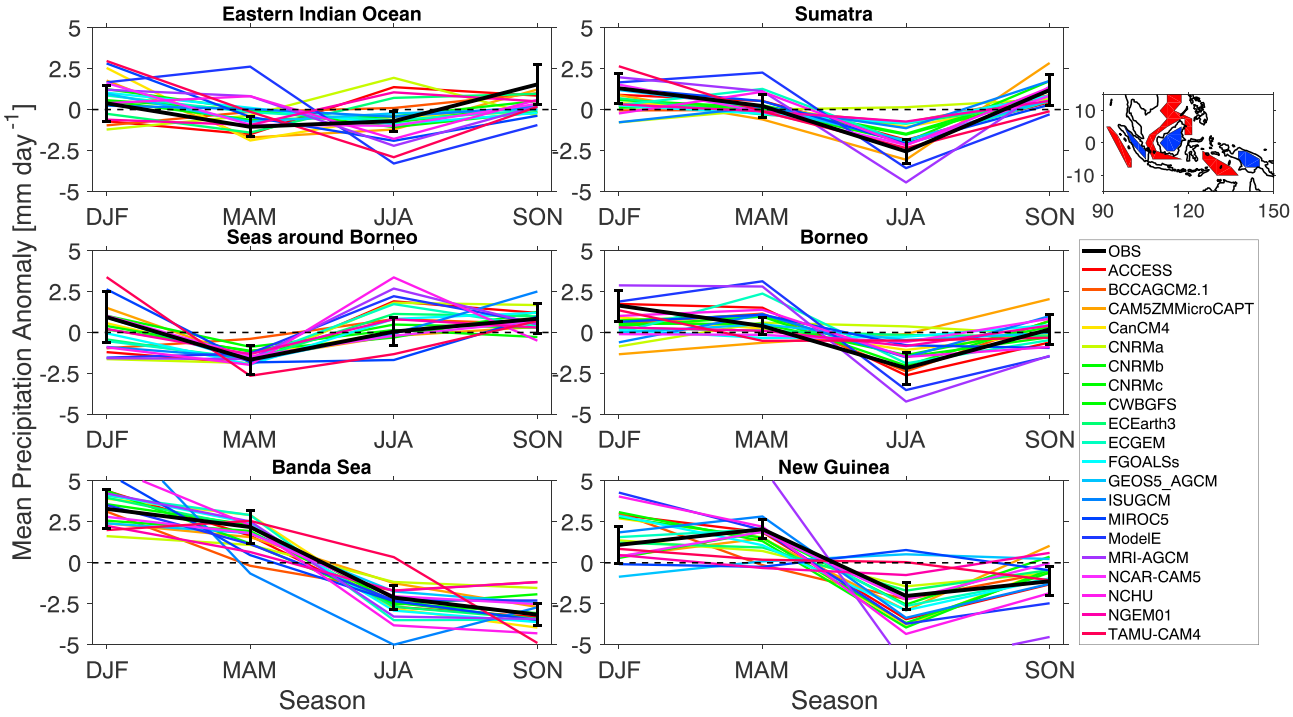

Figure 11. Seasonal cycle of the daily mean precipitation anomaly in GASS/MJOTF models over six regions (mm/day). Each line represents one model. Low-resolution TRMM observations are marked with thick black line; a standard deviation is calculated from all full seasons available and marked with a vertical bar. Each panel represents one region. The map in the upper right shows all ocean (red) and land (blue) regions analyzed in the figure. JJA = June–August; DJF = December–February; MAM = March–May; SON = September–November.

mean precipitation. Its magnitude is smallest over ocean regions of the eastern Indian Ocean and seas around Borneo. The seasonal variation there is below 3 mm/day. Over all land regions, the peak-to-peak seasonal change in the daily mean precipitation rate is between 3.5 and 4.0 mm/day. The Banda Sea exhibits the strongest seasonal modulation of daily mean precipitation, where the magnitude of the seasonal cycle exceeds 6 mm/day. The daily mean precipitation rate is smallest during boreal spring (March–May, MAM) and highest during boreal autumn (September–November, SON) and winter (December–February, DJF) over the eastern Indian Ocean and seas around Borneo. Over Sumatra and Borneo, the maximum precipitation is observed during the same season as over the surrounding seas, but the annual minimum occurs later—during boreal summer (June–August, JJA). Over the Banda Sea and New Guinea, precipitation during the first two seasons (DJF and MAM) is substantially larger than during the second half of the year. This shows an influence of the Australian monsoon on the eastern part of the MC region.

The models show overall reasonable performance with respect to the seasonal cycle of the daily mean precipitation. Although discrepancies with respect to the magnitude of the seasonal cycle are apparent over all regions, most models realistically represent wetter and drier seasons throughout the year. The biggest divergence between observation and models can be seen over the eastern Indian Ocean and seas around Borneo. About half of the models unrealistically show a maximum of the seasonal cycle during boreal summer (JJA), exceeding typical year-to-year variability observed in reference data set.

In comparison with the seasonal cycle of the daily mean precipitation, the observed seasonal cycle of the relative amplitude of the diurnal cycle of precipitation (Figure 12) shows very little variability. This is because the amplitude (full, not relative) of the diurnal cycle of precipitation and daily mean precipitation rate are correlated. This shows the importance of multiscale interactions over the MC region. The higher daily mean precipitation rates during wet seasons are clearly associated with the higher amplitude of the diurnal cycle.

In comparison with observations, models tend to exaggerate the seasonal cycle of the relative amplitude of the diurnal cycle. The best performance among models can be seen over the eastern Indian Ocean and the

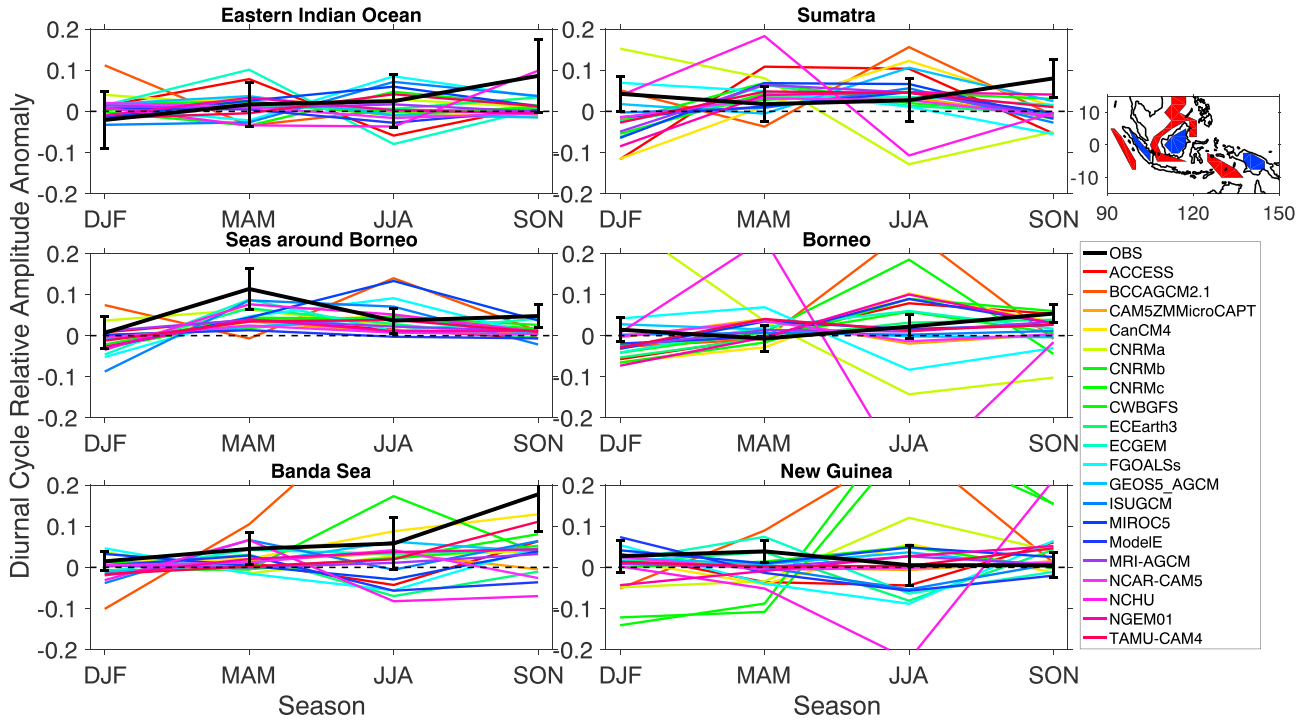

Figure 12. Seasonal cycle of the relative amplitude of the diurnal cycle in GASS/MJOTF models over six regions. Each line represents one model. Low-resolution TRMM observations are marked with thick black line; a standard deviation is calculated from all full seasons available and marked with a vertical bar. Each panel represents one region. The map in the upper right shows all ocean (red) and land (blue) regions analyzed in the figure. JJA = June–August; DJF = December–February; MAM = March–May; SON = September–November.

seas around Borneo, where many models show seasonal cycle within typical year-to-year variability observed in reality. Discrepancies between models and observations are largest over the Banda Sea, especially during boreal summer and fall, and over New Guinea. BCCAGCM2.1, NCHU, and the CNRM family perform particularly poorly in the latter regard, though the exaggerated seasonal cycle among them is not consistent. For example, BCCAGCM2.1, the only model in this group that largely underestimates the diurnal cycle amplitude over the MC region (Figure 7), strongly overestimates the seasonal amplitude of the diurnal cycle during boreal summer in comparison with the annual mean. On the other hand, the NCHU model has a strong seasonal cycle bias over land regions. Over Sumatra and Borneo it has diurnal cycle amplitude that is too large during MAM and too small during JJA. Over New Guinea the largest discrepancies between this model and the observed seasonal cycle are observed during boreal summer (suppressed diurnal cycle) and fall (enhanced diurnal cycle). Models from the CNRM family have the largest bias during boreal summer and winter. Interestingly, the magnitude and sign of the biases vary between different CNRM simulations. Coupled (CNRMb) and semicoupled (CNRMc) simulations have larger biases over New Guinea, whereas the atmosphere-only simulation (CNRMa) has substantially larger bias than other runs over Sumatra and Borneo.

Clear discrepancies between most models and observations suggest that, unlike in nature, the seasonal cycle of the amplitude (full, not relative) of the diurnal cycle in those models is not correlated with the daily mean precipitation. This suggests that multiscale interactions responsible for the link between seasonal variability in the daily mean precipitation rate and the amplitude of the diurnal cycle are not sufficiently represented in GCMs. In the case of BCCAGCM.2.1, which underperforms with respect to the amplitude of the diurnal cycle but reproduces some features of the seasonal cycle of the mean precipitation, this simply means that the diurnal modulation of the precipitation is small regardless of the season and daily mean precipitation. Such a representation is unrealistic because observations show a clear link between the amplitude of the diurnal cycle and daily mean precipitation.

The observations indicate that most regions exhibit a phase of the diurnal cycle that is consistent throughout the year (Figure 13). However, ocean regions exhibit much larger year-to-year variability. This is likely due to

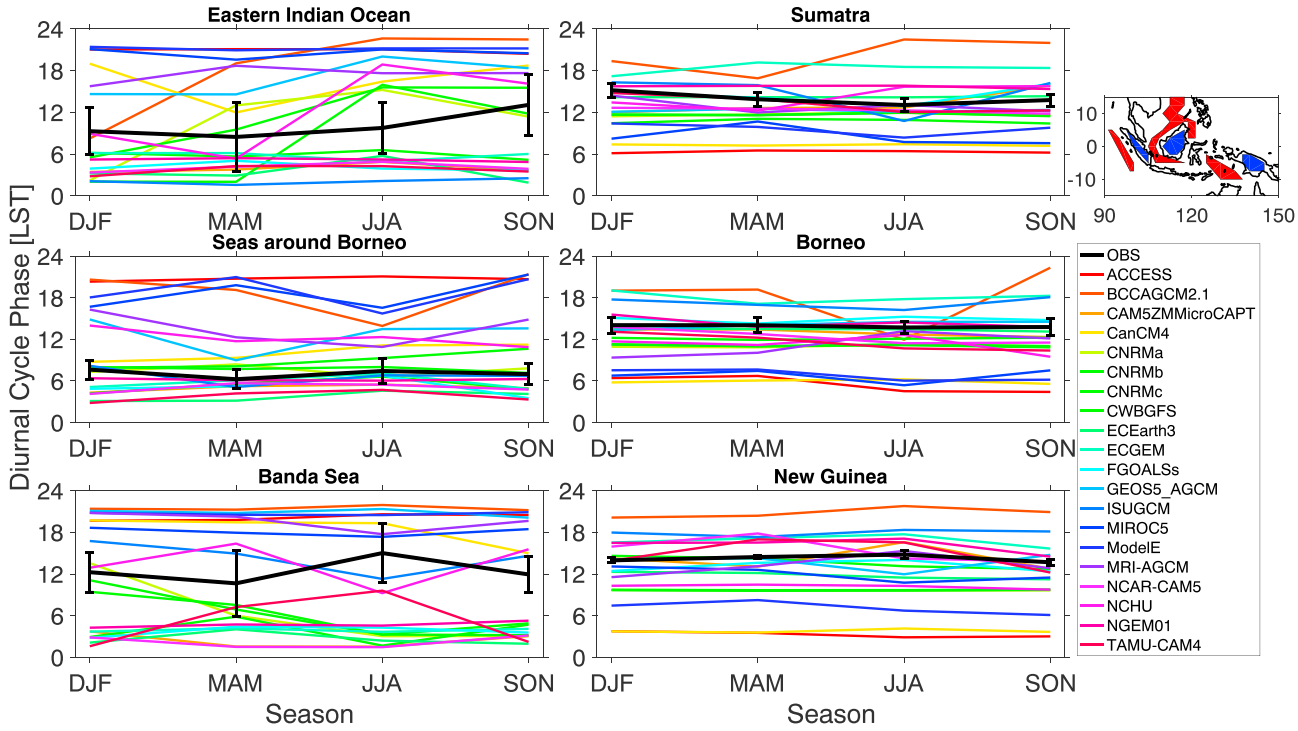

Figure 13. Seasonal cycle of the phase of the diurnal cycle in GASS/MJOTF models over six regions. Each line represents one model. Low-resolution TRMM observations are marked with thick black line; a standard deviation is calculated from all full seasons available and marked with a vertical bar. Each panel represents one region. The map in the upper right shows all ocean (red) and land (blue) regions analyzed in the figure. JJA = June–August; DJF = December–February; MAM = March–May; SON = September–November.

the fact that ocean region show overall weaker diurnal cycle and regions near the coast may show some blended ocean/land characteristics. Over the eastern Indian Ocean, the maximum precipitation occurs a little later during the day during JJA and SON than during DJF. Over the Banda Sea region, the maximum precipitation occurs 6 to 8 hr later during DJF and JJA than during other parts of a year. However, in both regions, magnitude of this seasonal cycle is smaller than its year-to-year variability. Most of the models exhibit constancy with respect to the phase of the diurnal cycle over all regions. This means that if a model produces diurnal cycle with a certain phase (correct or not), it maintains the same phase throughout the year. This constancy of phase is at least consistent with observations over most regions.

5. Summary and Discussion

In a previous assessment of GCM performance with respect to precipitation patterns over the MC, Neale and Slingo (2003) found that the MC exhibits a dry bias due to insufficient representation of the diurnal cycle of convection over the local complex topography. Despite constant progress in the representation of tropical convection and its variability in modern models (Hung et al., 2013; Jiang et al., 2015; Kim et al., 2009), multiscale interactions over the MC still impose substantial challenges to climate models (Love et al., 2011; Seo et al., 2009).

In this study we illustrate that the representation of the diurnal cycle of precipitation, a key component of multiscale interactions over the MC (Baranowski et al., 2016; Hagos et al., 2016; Peatman et al., 2014), in state-of-the-art GCMs is better than in past generations of weather and climate models (Neale & Slingo, 2003). Models are evaluated based on diurnal cycle metrics derived from high-resolution precipitation estimates as well as recalculated to match models' spatial and temporal resolution. It has been show that 6-hourly model outputs, while less than ideal, well capture key characteristics of the diurnal cycle such as amplitude and phase. Based on a number of diurnal cycle metrics (Figures 3 and 5), we show that although many models still underestimate the daily mean precipitation (Figure 6), especially over the eastern Indian

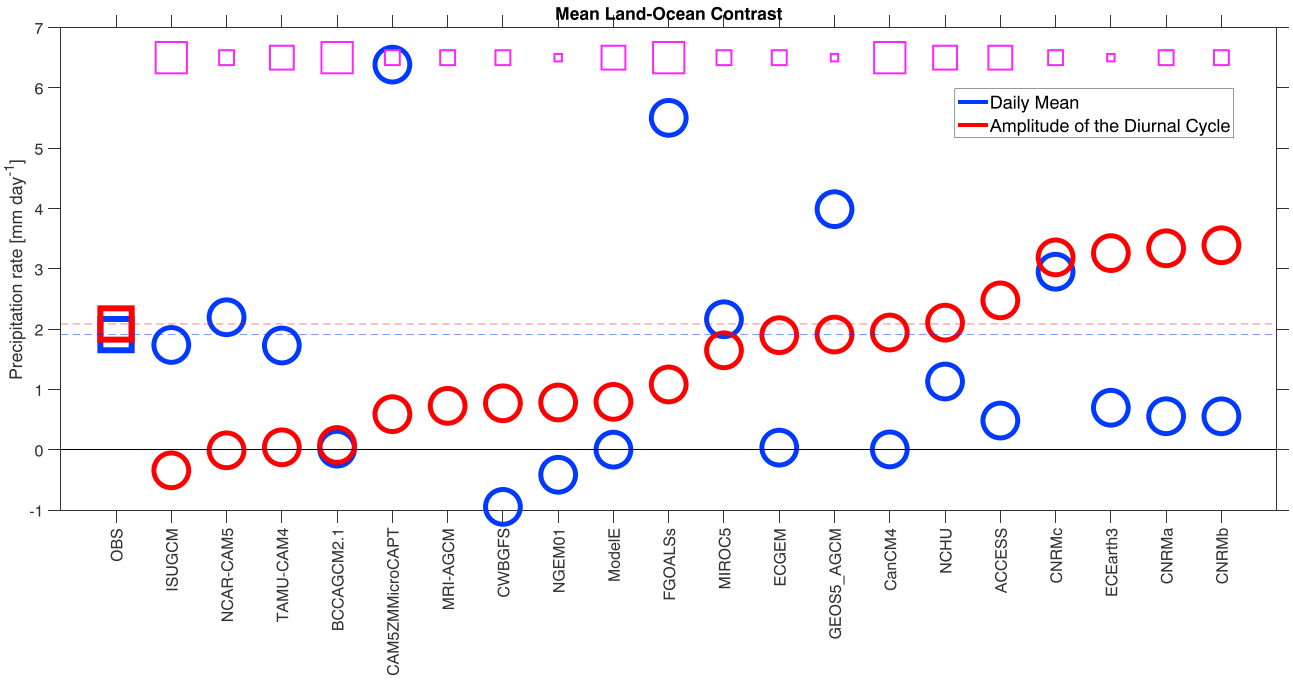

Figure 14. Land-Ocean contrast in GASS/MJOTF models and observations (low-resolution TRMM) calculated as average difference between land regions (Sumatra, Borneo, and New Guinea) and ocean regions (Eastern Indian Ocean, Seas around Borneo, and Banda Sea). Blue markers represent land-ocean contrast (mm/day) in daily mean precipitation, and red markers represent land-ocean contrast (mm/day) in total (NOT relative) amplitude of the diurnal cycle. Note that sequence of models is sorted by the land-ocean contrast in the amplitude of the diurnal cycle, and therefore, the order is different from previous figures. Magenta markers indicate models' native resolution; models are divided into four bins: 0–100 (smallest squares), 100–200, 200–300, and above 300 km (largest squares).

Ocean, some GCMs reproduce the daily mean precipitation relatively well. Observations show that both daily mean precipitation and amplitude of the diurnal cycle of precipitation are higher over the islands within the MC region than over adjacent seas, but models tend to decrease this land-sea contrast. Analysis of the phase of the diurnal cycle of precipitation (Figures 8 and 9) shows that all but one model represent the spatial variability of the peak hour of the diurnal precipitation consistent with the distribution of land and ocean within the region. This means that models in general are sensitive to the existence of islands within the region. On the other hand, more than half of the GCMs studied here fail to correctly reproduce the phase of the diurnal cycle, especially over land where precipitation often occurs too early in comparison with observations. The fact that the hour of maximum precipitation is better represented over the ocean points to problems with parameterization of convection and/or surface processes in models as well as to the spatial resolution not being able to represent the fine topographic features of the MC islands (Love et al., 2011). At the same time, some models show substantial improvement in comparison with previous generations and their performance is similar to mesoscale model simulations run in much higher resolutions (Hassim et al., 2016).

Analysis of the amplitude of the diurnal cycle (Figure 7) shows some consistency in underestimation of the diurnal variation of precipitation, especially over land. However, 9 out of 20 GCMs show a higher amplitude of the diurnal cycle over the islands in comparison with observations. In fact, those models maintain or even increase the land-ocean contrast in the diurnal variation of precipitation (Figure 14). On the other hand, there is no consistency between land-sea contrast in the daily mean precipitation and amplitude of the diurnal cycle of precipitation among GCMs investigated in this study. Many models show increased (decreased) land-sea contrast in the daily mean precipitation but decreased (increased) contrast in the amplitude of the diurnal cycle of precipitation (Figure 14). This is unrealistic because observations show that the two are correlated; namely, when the daily mean precipitation increases, the amplitude of the diurnal cycle also increases. Such feature is exemplified by the high correlation of observed seasonal cycles of daily mean precipitation and the amplitude of the diurnal cycle and the resulting small seasonal variability of A_r (Figure 12).

GCMs' inability to represent this relationship points to the systematic failure in proper representation of multiscale interactions.

Another aspect is a weak relationship between model's resolution and its fidelity in representing the diurnal cycle. In the current study all model outputs were interpolated onto a common grid, which may have contributed to the observed biases. Nevertheless, models were run in the whole spectrum of native resolutions (from less than 50 km to more than 300 km). Although some of models worst performing with respect to the land-sea contrast (ISUGCM and BCCAGCM2.1) were run with coarse native resolution (>300 km), FGOALSs and CanCM4 (which were had equally coarse native resolution) performed much better. This result agrees with an assessment of previous generation models' performance with respect to the diurnal cycle over the MC (Neale & Slingo, 2003) as well as recent study that focused on the annual cycle of precipitation over the region (Toh et al., 2018).

Among the three coupled simulations out of the total of 20 model runs, two of them exhibit relatively better performance with respect to the land-sea contrast in the amplitude of the diurnal cycle. Particularly, analysis of the atmosphere-only and coupled runs from CNRM models (runs a and b) shows that in this modeling system coupling with the ocean model improves both the daily mean precipitation rate and the amplitude of the diurnal cycle and has no influence on the phase of the diurnal cycle. Another coupled model (CanCM4), however, shows unrealistic, reversed land-sea contrast in the daily mean precipitation. Our results point to the continued need to better understand, possibly through the ongoing Year of the Maritime Continent (http://www.jamstec.go.jp/ymc/docs/YMC_SciencePlan_v2.pdf) and Propagation of Intra-Seasonal Tropical Oscillations (https://www.onr.navy.mil/Science-Technology/Departments/Code-32/All-Programs/Atmosphere-Research-322/Marine-Meteorology-Atmospheric-Effects/Intra-Seasonal-Tropical-Oscillations-DRI.aspx) field campaigns, and model these multiscale interactions and the processes that lead to the diurnal cycle in particular.

Acknowledgments
The multimodel output collected by this project and analyzed in this study is available for free download from https://earthsystemcog.org/projects/gassyotc-mip/. D. B. B. acknowledges support from the Office of Naval Research (award N000141210580 to the UCLA). D. W .acknowledges support from the Jet Propulsion Laboratory, California Institute of Technology, under a contract with the National Aeronautics and Space Administration. X. J. acknowledges support by NOAA Climate Program Office under awards NA15OAR4310098 and NA15OAR4310177. In addition, support from the Office of Naval Research Program Element 0601153N is also gratefully acknowledged.

References

Ackerley, D., Berry, G., Jakob, C., & Reeder, M. J. (2014). The roles of diurnal forcing and large-scale moisture transport for initiating rain over northwest Australia in a GCM. *Quarterly Journal of the Royal Meteorological Society*, *140*(685), 2515–2526. https://doi.org/10.1002/qj.2316

Baranowski, D. B., Flatau, M. K., Flatau, P. J., & Matthews, A. J. (2016). Phase locking between atmospheric convectively coupled equatorial Kelvin waves and the diurnal cycle of precipitation over the Maritime Continent. *Geophysical Research Letters*, *43*, 8269–8276. https://doi.org/10.1002/2016GL069602

Birch, C. E., Webster, S., Peatman, S. C., Parker, D. J., Matthews, A. J., Li, Y., & Hassim, M. E. E. (2016). Scale interactions between the MJO and the Western Maritime Continent. *Journal of Climate*, *29*(7), 2471–2492. https://doi.org/10.1175/JCLI-D-15-0557.1

Chen, S. S., & Houze, R. A. (1997). Diurnal variation and life-cycle of deep convective systems over the tropical Pacific warm pool. *Quarterly Journal of the Royal Meteorological Society*, *123*(538), 357–388. https://doi.org/10.1002/qj.49712353806

Dai, A. (2001). Global precipitation and thunderstorm frequencies, Part I: Seasonal and interannual variations. *Journal of Climate*, *14*(6), 1092–1111. https://doi.org/10.1175/1520-0442(2001)014<1092:GPATFP>2.0.CO;2

Gray, W. M., & Jacobson, R. W. (1977). Diurnal variation of deep cumulus convection. *Monthly Weather Review*, *105*(9), 1171–1188. https://doi.org/10.1175/1520-0493(1977)105<1171:DVODCC>2.0.CO;2

Hagos, S. M., Zhang, C., Feng, Z., Burleyson, C. D., De Mott, C., Kerns, B., et al. (2016). The impact of the diurnal cycle on the propagation of MJO convection across the Maritime Continent. *Journal of Advances in Modeling Earth Systems*, *8*, 1552–1564. https://doi.org/10.1002/2016MS000725

Hassim, M. E. E., Lane, T. P., & Grabowski, W. W. (2016). The diurnal cycle of rainfall over New Guinea in convection-permitting WRF simulations. *Atmospheric Chemistry and Physics*, *16*(1), 161–175. https://doi.org/10.5194/acp-16-161-2016

Huffman, G. J., Adler, R. F., Bolvin, D. T., Gu, G., Nelkin, E. J., Bowman, K. P., et al. (2007). The TRMM multisatellite precipitation analysis (TMPA): Quasi-global, multiyear, combined-sensor precipitation estimates at fine scales. *Journal of Hydrometeorology*, *8*(1), 38–55. https://doi.org/10.1175/jhm560.1

Hung, M.-P., Lin, J.-L., Wang, W., Kim, D., Shinoda, T., & Weaver, S. J. (2013). MJO and convectively coupled equatorial waves simulated by CMIP5 climate models. *Journal of Climate*, *26*(17), 6185–6214. https://doi.org/10.1175/JCLI-D-12-00541.1

Jiang, X., Waliser, D. E., Xavier, P. K., Petch, J., Klingaman, N. P., Woolnough, S. J., et al. (2015). Vertical structure and physical processes of the Madden-Julian Oscillation: Exploring key model physics in climate simulations. *Journal of Geophysical Research: Atmospheres*, *120*, 4718–4748. https://doi.org/10.1002/2014JD022375

Kim, D., Sperber, K., Stern, W., Waliser, D., Kang, I. S., Maloney, E., et al. (2009). Application of MJO simulation diagnostics to climate models. *Journal of Climate*, *22*(23), 6413–6436. https://doi.org/10.1175/2009JCLI3063.1

Klingaman, N. P., Jiang, X., Xavier, P. K., Petch, J., Waliser, D., & Woolnough, S. J. (2015). Vertical structure and physical processes of the Madden-Julian Oscillation: Synthesis and summary. *Journal of Geophysical Research: Atmospheres*, *120*, 4671–4689. https://doi.org/10.1002/2015JD023196

Klingaman, N. P., Woolnough, S. J., Jiang, X., Waliser, D., Xavier, P. K., Petch, J., et al. (2015). Vertical structure and physical processes of the Madden-Julian Oscillation: Linking hindcast fidelity to simulated diabatic heating and moistening. *Journal of Geophysical Research: Atmospheres*, *120*, 4690–4717. https://doi.org/10.1002/2014JD022374

Lappen, C.-L., & Schumacher, C. (2012). Heating in the tropical atmosphere: What level of detail is critical for accurate MJO simulations in GCMs? *Climate Dynamics*, *39*(9-10), 2547–2568. https://doi.org/10.1007/s00382-012-1327-y

Lappen, C.-L., & Schumacher, C. (2014). The role of tilted heating in the evolution of the MJO. *Journal of Geophysical Research: Atmospheres*, *119*, 2966–2989. https://doi.org/10.1002/2013JD020638

Lau, W. K. M., & Waliser, D. E. (Eds.) (2011). *Intraseasonal variability of the atmosphere-ocean climate system* (2nd ed., p. 613). Heidelberg, Germany: Springer Praxis Books.

Love, B. S., Matthews, A. J., & Lister, G. M. S. (2011). The diurnal cycle of precipitation over the Maritime Continent in a high-resolution atmospheric model. *Quarterly Journal of the Royal Meteorological Society*, *137*(657), 934–947. https://doi.org/10.1002/qj.809

Madden, R. A., & Julian, P. R. (1972). Description of global-scale circulation cells in the tropics with a 40–50 day period. *Journal of the Atmospheric Sciences*, *29*(6), 1109–1123. https://doi.org/10.1175/1520-0469(1972)029<1109:DOGSCC>2.0.CO;2

Matthews, A. J., Pickup, G., Peatman, S. C., Clews, P., & Martin, J. (2013). The effect of the Madden-Julian Oscillation on station rainfall and river level in the Fly River system, Papua New Guinea. *Journal of Geophysical Research: Atmospheres*, *118*, 10,926–10,935. https://doi.org/10.1002/jgrd.50865

Mori, S., Hamada, J. I., Tauhid, Y. I., Yamanaka, M. D., Okamoto, N., Murata, F., et al. (2004). Diurnal land-sea rainfall peak migration over Sumatera Island, Indonesian Maritime Continent, observed by TRMM satellite and intensive rawinsonde soundings. *Monthly Weather Review*, *132*(8), 2021–2039. https://doi.org/10.1175/1520-0493(2004)132<2021:dlrpmo>2.0.co;2

Neale, R., & Slingo, J. (2003). The Maritime Continent and its role in the global climate: A GCM study. *Journal of Climate*, *16*(5), 834–848. https://doi.org/10.1175/1520-0442(2003)016<0834:tmcair>2.0.co;2

Neena, J. M., Lee, J. Y., Waliser, D., Wang, B., & Jiang, X. (2014). Predictability of the Madden–Julian Oscillation in the Intraseasonal Variability Hindcast Experiment (ISVHE). *Journal of Climate*, *27*(12), 4531–4543. https://doi.org/10.1175/JCLI-D-13-00624.1

Oh, J.-H., Kim, K.-Y., & Lim, G.-H. (2012). Impact of MJO on the diurnal cycle of rainfall over the western Maritime Continent in the austral summer. *Climate Dynamics*, *38*(5-6), 1167–1180. https://doi.org/10.1007/s00382-011-1237-4

Peatman, S. C., Matthews, A. J., & Stevens, D. P. (2014). Propagation of the Madden–Julian Oscillation through the Maritime Continent and scale interaction with the diurnal cycle of precipitation. *Quarterly Journal of the Royal Meteorological Society*, *140*(680), 814–825. https://doi.org/10.1002/qj.2161

Petch, J., Waliser, D., Jiang, X., Xavier, P., & Woolnough, S. (2011). A global model intercomparison of the physical processes associated with the Madden–Julian Oscillation, GEWEX News, August.

Pritchard, M. S., & Somerville, R. C. J. (2009). Assessing the diurnal cycle of precipitation in a multi-scale climate model. *Journal of Advances in Modeling Earth Systems*, *1*, 12. https://doi.org/10.3894/JAMES.2009.1.12

Qian, J.-H. (2008). Why precipitation is mostly concentrated over islands in the Maritime Continent. *Journal of the Atmospheric Sciences*, *65*(4), 1428–1441. https://doi.org/10.1175/2007JAS2422.1

Ramage, C. S. (1968). Role of a tropical "Maritime Continent" in the atmospheric circulation. *Monthly Weather Review*, *96*(6), 365–370. https://doi.org/10.1175/1520-0493(1968)096<0365:ROATMC>2.0.CO;2

Reichler, T., & Roads, J. O. (2005). Long-range predictability in the tropics. Part II: 30–60-day variability. *Journal of Climate*, *18*(5), 634–650. https://doi.org/10.1175/JCLI-3295.1

Reynolds, R. W., Rayner, N. A., Smith, T. M., Stokes, D. C., & Wang, W. Q. (2002). An improved in situ and satellite SST analysis for climate. *Journal of Climate*, *15*(13), 1609–1625. https://doi.org/10.1175/1520-0442(2002)015<1609:Aiisas>2.0.Co;2

Rui, H., & Wang, B. (1990). Development characteristics and dynamic structure of tropical intraseasonal convection anomalies. *Journal of the Atmospheric Sciences*, *47*(3), 357–379. https://doi.org/10.1175/1520-0469(1990)047<0357:DCADSO>2.0.CO;2

Ruppert, J. H. J., & Hohenegger, C. (2018). Diurnal circulation adjustment and organized deep convection. *Journal of Climate*, *31*(12), 4899–4916. https://doi.org/10.1175/jcli-d-17-0693.1

Salby, M. L., & Hendon, H. H. (1994). Intraseasonal behavior of clouds, temperature, and motion in the tropics. *Journal of the Atmospheric Sciences*, *51*(15), 2207–2224. https://doi.org/10.1175/1520-0469(1994)051<2207:IBOCTA>2.0.CO;2

Seo, K.-H., Wang, W., Gottschalck, J., Zhang, Q., Schemm, J.-K. E., Higgins, W. R., & Kumar, A. (2009). Evaluation of MJO forecast skill from several statistical and dynamical forecast models. *Journal of Climate*, *22*(9), 2372–2388. https://doi.org/10.1175/2008jcli2421.1

Thompson, B., Sanchez, C., Sun, X., Song, G., Liu, J., Huang, X.-Y., & Tkalich, P. (2018). A high-resolution atmosphere–ocean coupled model for the western Maritime Continent: Development and preliminary assessment. *Climate Dynamics*. https://doi.org/10.1007/s00382-018-4367-0

Toh, Y. Y., Turner, A. G., Johnson, S. J., & Holloway, C. E. (2018). Maritime Continent seasonal climate biases in AMIP experiments of the CMIP5 multimodel ensemble. *Climate Dynamics*, *50*(3-4), 777–800. https://doi.org/10.1007/s00382-017-3641-x

Waliser, D. E., Stern, W., Schubert, S., & Lau, K. M. (2003). Dynamic predictability of intraseasonal variability associated with the Asian summer monsoon. *Quarterly Journal of the Royal Meteorological Society*, *129*(594), 2897–2925. https://doi.org/10.1256/qj.02.51

Wallace, J. M. (1975). Diurnal variations in precipitation and thunderstorm frequency over the conterminous United States. *Monthly Weather Review*, *103*(5), 406–419. https://doi.org/10.1175/1520-0493(1975)103<0406:DVIPAT>2.0.CO;2

Wang, S., & Sobel, A. H. (2017). Factors controlling rain on small tropical islands: Diurnal cycle, large-scale wind speed, and topography. *Journal of the Atmospheric Sciences*, *74*(11), 3515–3532. https://doi.org/10.1175/jas-d-16-0344.1

Xavier, P. K., Petch, J. C., Klingaman, N. P., Woolnough, S. J., Jiang, X., Waliser, D. E., et al. (2015). Vertical structure and physical processes of the Madden-Julian Oscillation: Biases and uncertainties at short range. *Journal of Geophysical Research: Atmospheres*, *120*, 4749–4763. https://doi.org/10.1002/2014JD022718

Zhang, C. (2005). Madden-Julian Oscillation. *Reviews of Geophysics*, *43*, RG2003. https://doi.org/10.1029/2004RG000158